LBL-14752

LBL--14752

DE83 004100

THERMAL-GRADIENT MIGRATION OF BRINE INCLUSIONS IN SALT CRYSTALS

Suresh Kumar Yagnik
Ph.D. Thesis

Lawrence Berkeley Laboratory
University of California
Berkeley, California 94720

This work was supported by the Director, Office of Energy Research, Office of Basic Energy Sciences, Materials Sciences Division of the U. S. Department of Energy under Contract No. DE-AC03-76SF00098

CONTENTS

Page

THERMAL-GRADIENT MIGRATION OF BRINE INCLUSIONS IN SALT CRYSTALS

Suresh Kumar Yagnik

Materials and Molecular Research Division
Lawrence Berkeley Laboratory
University of California
Berkeley, California 94720

ABSTRACT

It has been proposed that high-level nuclear waste be disposed in a geologic repository. Natural-salt deposits, which are being considered for this purpose, contain a small volume fraction of water in the form of brine inclusions distributed throughout the salt. Radioactive-decay heating of the nuclear wastes will impose a temperature gradient on the surrounding salt which mobilizes the brine inclusions. Inclusions filled completely with brine (the all-liquid inclusions) migrate up the temperature gradient and eventually accumulate brine near the buried waste forms. The brine may slowly corrode or degrade the waste forms which is undesirable.

The inclusions were trapped when the salt originally crystallized some 200 million years ago. Inclusions of various sizes and shapes occur in natural salt. Often the inclusions may contain a gas phase such as water vapor, H_2S, CH_4, or N_2. This type of inclusions migrate down the temperature gradient. It is possible that the gas-liquid inclusions may act as a pathway for radionuclides leached from the wastes to the biosphere.

Therefore it is important to consider the migration of brine inclusions in salt under imposed temperature gradients to properly evaluate the performance of a future salt repository for nuclear wastes.

In the present work, thermal gradient migration of both all-liquid and gas-liquid inclusions was experimentally studied in synthetic single crystals of NaCl and KCl using a hot-stage attachment to an optical microscope which was capable of imposing temperature gradients and axial compressive loads on the crystals. The migration velocities of the inclusions were found to be dependent on temperature, temperature gradient, and inclusion shape and size. The velocities were also dictated by the interfacial mass transfer resistance at brine/solid interface. This interfacial resistance depends on the dislocation density in the crystal, which in turn, depends on the axial compressive loading of the crystal. At low axial loads, the dependence between the velocity and temperature gradient is non-linear. At high axial loads, however, the interfacial resistance is reduced and the migration velocity depends linearly on the temperature gradient.

All-liquid inclusions filled with mixed brines were also studied. For gas-liquid inclusions, three different gas phases (helium, air and argon) were compared. Migration studies were also conducted on single crystallites of natural salt as well as in polycrystalline natural salt samples. The behavior of the inclusions at large angle grain boundaries was observed.

ACKNOWLEDGEMENTS

The author wishes to express his deep gratitude to his research advisor Professor Donald R. Olander, Department of Nuclear Engineering, University of California at Berkeley for constant guidance and encouragement throughout this work. Professor Olander's suggestions on the experiments, theory, and data analysis were of immense value.

The author is indebted to Professor Albert J. Machiels, Nuclear Engineering Program, University of Illinois, Urbana who spent over a year at Berkeley and extended his guidance and friendly assistance to the author during the early stage of this work.

Thanks are also due to Dr. Mehdi Balooch for initiating the experimental work and for many helpful discussions.

Mr. Greg Mitchem prepared the helium-water and argon-water samples for migration experiments. Gloria Pelatowski skillfully prepared the line drawings.

The assistance of the entire technical staff of the department is thankfully acknowledged. In particular Dan Winterbauer, John Souza, and Jack Harrell efficiently fabricated and assembled the experimental set-up.

This research work was supported by the Office of Nuclear Waste Isolation, Battelle, Columbus (Ohio).

LIST OF FIGURES

LIST OF TABLES

CHAPTER 1

INTRODUCTION

The method of disposing of high level nuclear wastes which is being actively considered around the world is that of construction of a nuclear waste repository. Under this plan, the nuclear waste canisters will be lowered and buried deep underground in a suitable geologic medium. The basic philosophy of geologic disposal is to isolate the nuclear waste from the biosphere. The integrity of the waste canisters must be guaranteed for as long as the wastes remain toxic and hazardous (typically 1000 years).

In addition to the high levels of radioactivity, the wastes generate decay heat. When such wastes are buried, they impose a temperature gradient on the surrounding geologic rock. The waste canisters must be designed to maintain their integrity under the conditions of stress, irradiation, temperature, and temperature gradient which will exist in a future nuclear repository. All possible physical and chemical interactions between the host rock and the waste packages must be considered.

The selection of the geologic medium depends on the seismicity and ground water occurrence. The host rock should exhibit low porosity, low plasticity and high thermal conductivity [1]. Bedded and domed natural salt deposits meet most of these requirements and are the prime candidates for future nuclear waste repository.

The salt deposits, however, contain brine inclusions distributed throughout the medium [2]. The inclusions were trapped when salt deposits originally crystallized from sea water some 200 million years

ago. These inclusions will be mobilized by the thermal gradient generated by the decay heat of the nuclear wastes buried in a salt repository.

The inclusions are essentially pockets of brine trapped inside the solid rock salt. They are found in the size range of a few micrometers to several millimeters [2,3]. In one study [3] of samples of bedded salt from New Mexico, the average fluid content varied from ~0.1 to 1.7 weight percent (roughly ~0.2 to 3.0 volume percent). The fluid content in domed salt deposits is found to be generally lower than bedded salt deposits, usually in the range of 0.01 to 0.001 volume percent [4].

The composition of the brine in inclusions is found to vary from one salt deposit to the other. Most analyses show that the brines contain Ca^{++} and Mg^{++} ions in addition to varying amounts of Na^{+}, Cl^{-}, and SO_4^{--} [2]. Samples of brine inclusions in the bedded salt at Hutchinson, Kansas were found to contain 2.1 molar $MgCl_2$ and 1.9 molar NaCl, with small amounts [5] of Ca^{++}, Br^{-}, SO_4^{--}, and K^{+}.

Most inclusions observed in natural salt are filled completely with brine (the all-liquid inclusions). Occasionally, however, a gas phase is also present within the brine. This may have resulted from the reappearance of dissolved gases upon cooling of the Earth's crust since the salt deposits originally formed. It is also speculated [6] that the gas phase may have appeared in the inclusions due to decomposition of mineral impurities such as carbonates in the rock salt. The gas in these inclusions is generally composed of water vapor, CO_2, CH_4, N_2, and H_2S.

Under an imposed thermal gradient, both the types of inclusions are set into motion within the host solid. While all-liquid inclusions move up the temperature gradient, the gas-liquid inclusions generally move down the gradient.

The motion of brine inclusions under a thermal gradient naturally raises concern about suitability of salt deposits for a nuclear waste repository. The all-liquid inclusions distributed throughout the salt formation will migrate towards the waste canisters under the influence of the temperature gradient generated by the decay heat of the wastes. Resulting accumulation of brine near the canisters may cause corrosion and leaching of radionuclides. Since gas-liquid inclusions move down the temperature gradient, it is conceivable that they could act as a pathway for the leached nuclides to the biosphere. Therefore, it is important to consider the migration of each kind of inclusion to properly evaluate performance of future nuclear repository in salt.

Thermomigration of brine inclusions was studied in high purity synthetic single crystals of NaCl and KCl as well as in natural salt. Gas-liquid inclusions with different gas phases were introduced into single crystals of NaCl and migration experiments were subsequently conducted on them.

The mechanism of migration of both types of inclusions is discussed in Chapter 2. The experimental techniques used in this work are described in Chapter 3. Chapter 4 contains the theory of thermomigration of all-liquid inclusions. The interfacial stability of the migrating

all-liquid inclusions is treated theoretically in Chapter 5. In Chapter 6 experimental results are discussed. Finally, in Chapter 7 the conclusions of this work are given.

CHAPTER 2

THE MECHANISM OF THERMOMIGRATION

When an external potential gradient is applied to a solid containing inclusions, a directed motion is induced in inclusions. Such motion in a variety of potential gradients is of great academic interest and has many technological consequences. Under the influence of a temperature gradient, pores in ceramic nuclear fuels move up the gradient and affect the fuel element performance [7]. Inclusions in metals can be set into motion by the application of an external electric field [8]. Experimental evidence and theoretical treatments of the inclusion migration under other potential gradients such as accelerational fields and stress gradients are also summarized in reference [8].

A review of the mechanism of thermal gradient migration of all-liquid and gas-liquid inclusions in single crystals of alkali halides such as NaCl and KCl is presented below.

2.1. ALL-LIQUID INCLUSIONS

An inclusions can be viewed as a negative crystal of the host solid. Since alkali halides such as NaCl and KCl have a cubic crystal structure, the inclusions originally exhibit cubic shape. However, when an external temperature gradient is applied to the host crystal, the inclusions undergo a shape change. Most all-liquid inclusions take up a square platelet shape by flattening out in the direction of the applied gradient. The shape change process is thermodynamically analysed by Olander and coworkers [9].

The mechanism responsible for migration of all-liquid inclusions is discussed in literature by Anthony and Cline [10] and Geguzin and coworkers [11]. Figure 2A shows an all-liquid inclusion of width L in a salt crystal supporting a temperature gradient. Since the thermal conductivity of the solid is higher than that of liquid brine, the temperature gradient within the liquid, ∇T_l, is different from the applied gradient to the solid, ∇T_∞. The solubility of salt in water increases with temperature; therefore, the brine adjacent to the hot face of the inclusion has a higher concentration of dissolved salt than the brine adjacent to the cold face (i.e., $C_h^{sat} > C_c^{sat}$).

All-liquid inclusions migrate by the diffusional transport of dissolved salt from the hot face of the cavity to the cold face. In a temperature gradient, salt dissolves at the hot face, diffuses through the brine by molecular and thermal diffusion, and crystallizes out at the cold face. Consequently, the inclusion moves up the temperature gradient.

It should be noted that the interfacial mass transfer (i.e., the processes of solid dissolution into brine at the hot face and crystallization from the brine at the cold face) occurs in series with the thermal and molecular diffusion in brine. The kinetics of interfacial mass transfer is an important factor which, in addition to the diffusional transport of salt in the cavity, determines the velocity of migration of an inclusion. This will be discussed further in Chapter 4.

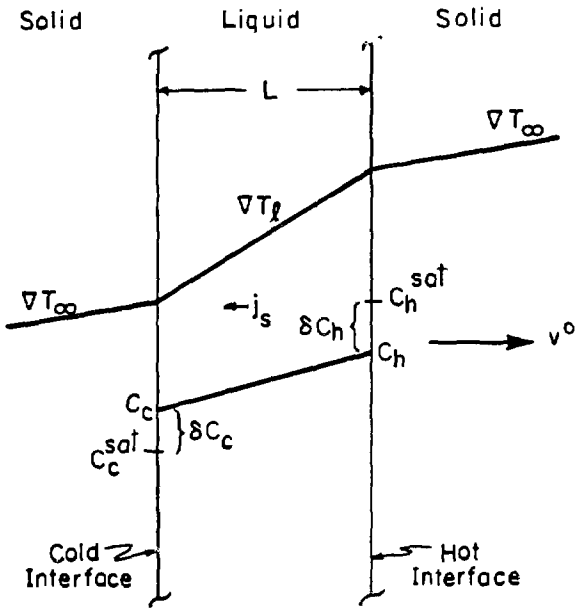

XBL827-6057

Fig. 2A. Section of an all-liquid inclusion in a solid supporting a temperature gradient.

2.2. GAS-LIQUID INCLUSIONS

Gas-liquid inclusions are generally cubic in shape with the gas bubble within the brine (Figure 2B). However, gas-liquid inclusions of several different shapes were observed in the present work, and the bubble is generally not centrally located during migration.

The mechanism of thermomigration of these inclusions is reported by Anthony and Cline [12] and Olander and coworkers [13]. Due to the increase in vapor pressure of water over brine with temperature, water evaporates from the hot side of the gas bubble and is transported to the cold side where it condenses. The condensed water is recycled to the hot side by backflow of brine which provides a means of moving dissolved salt from the cold face of the inclusion to the hot face. The change in temperature also causes a difference in the surface tension of the gas/brine interface. This results in a drag force on the brine in the annulus around the gas bubble.

Of course, the physical phenomenon of increase in solubility of salt with temperature, which gives rise to a diffusional transport of the brine from the hot brine/solid interface to the cold brine/solid interface, also operates here and results in a dissolved salt flux in the direction opposite to the backflow. However, depending on the phase volume ratio, the backflow effect overwhelms the solubility-driven salt flux and the net transport of dissolved salt is from the cold side of the cavity to the hot side. Consequently, for gas volume fractions > 0.1, gas-liquid inclusions move down the temperature gradient -- from the hot regions of the host solid crystal to the cold regions.

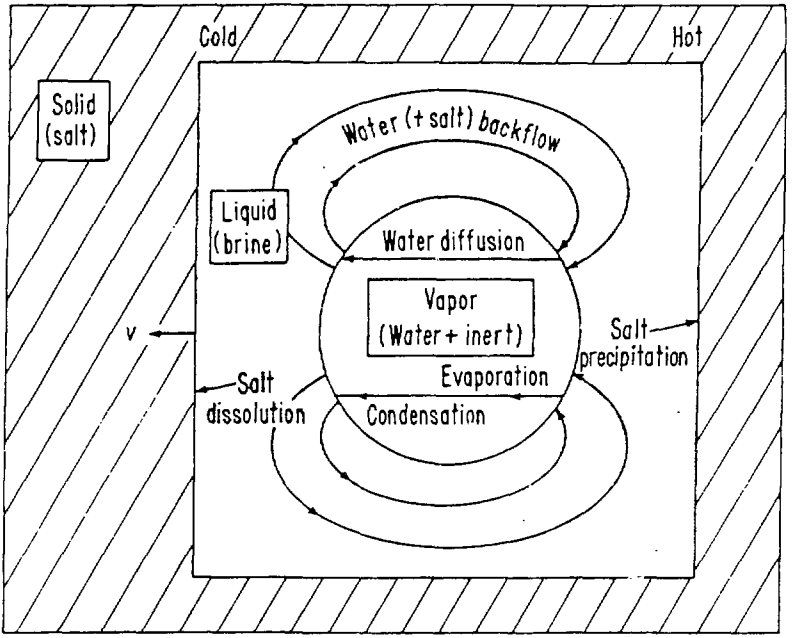

Fig. 2B. Schematic of the migration mechanism of gas-liquid inclusions in a temperature gradient.

CHAPTER 3

EXPERIMENTAL

3.1. SAMPLE PREPARATION

3.1.1 Synthetic Crystals

High purity crystals of NaCl and KCl of 15 mm x 5 mm x 5 mm size with <100>, <110>, and <111> crystallographic orientation were obtained from the Harshaw Chemical Company.

All-liquid inclusions are produced by drilling a 0.3 mm diameter and 3 mm deep hole in an end face of the crystal. The hole is filled with deionized water (or mixed brine, as the case may be), and the crystal is sandwiched with a rubber sheet and placed between two copper blocks maintained at different temperatures. The rubber sheet prevents evaporation of the liquid in the hole. By applying a temperature gradient of about 10° to 30°C/cm for five to fifteen days, all-liquid inclusions with a size distribution ranging from 7 to 200 μm can be produced. Because the inclusions conform to {100} planes, they are parallelepipeds when a temperature gradient is applied along a <100> direction. When the temperature gradient is applied in a different crystallographic direction, the shapes of the inclusions is more complex (chevron type), but the velocities are not significantly different from those in <100> directions for the same temperature gradient.

Gas-liquid inclusions are produced by essentially the same method but the direction of the applied temperature gradient used to create micron-size inclusions from the liquid-filled hole is reversed. In

other words, the end face of the crystal which is drilled and filled with deionized water is kept at a higher temperature from the other end face. The water and air trapped inside the drilled hole spawn gas-liquid inclusions (with air as the gas phase) in about two weeks time.

Figure 3A shows several inclusions of both kinds. The all-liquid inclusions are transparent platelets whereas gas-liquid inclusions are of several different shapes with a bubble of gas trapped in brine within a roughly cubic cavity.

Fabricating gas-liquid inclusions with helium or argon as the gas phase was more complex. For this purpose, an air-tight glove box was constructed through which high purity gas (helium or argon) was flushed. The glove box was equipped with a hot stage capable of applying a temperature gradient to the crystal into which the inclusions were to be introduced. A vial of deionized water, the drilled crystal, several drill bits (of the same size as the hole) were also placed inside the glove box before the gas flushing began. Initially during the gas flushing, the drilled hole on the crystal end face was scraped several times with the drill bits at regular intervals to ensure removal of the air from the hole. Since the crystal was drilled outside the glove box, the hole is likely to have some trapped air.

After about two days, a drop of deionized water was pushed into the hole on the crystal end face. The hole was sealed to prevent evaporation of the water and placed in a temperature gradient using the hot stage. The crystal was then allowed to stand the temperature

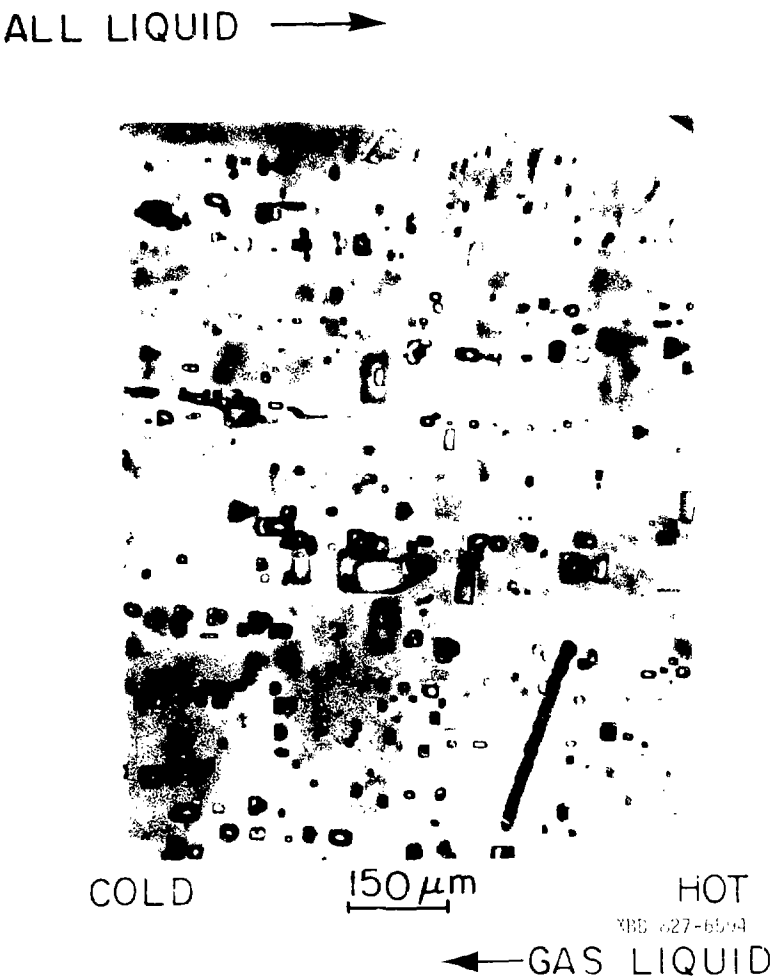

Fig. 3A. A photomicrograph of all-liquid and gas-liquid inclusions in a synthetic salt crystal.

gradient with continuous flushing of the gas. As before, in about two weeks time, the crystal had several trapped gas-liquid inclusions.

3.1.2 Natural Salt

Several large semi-transparent specimens of natural salt, dug from a depth of from 796 feet from Richton Dome salt formation, were tested. Unlike metals, the grains of natural salt are weakly bound and the specimen could easily be broken into smaller pieces by shearing. Careful procedures had to be used to machine the specimens to the desired sample size (15 mm x 5 mm x 5 mm). To enhance transparency, the surfaces of the machined samples were cleaned with a mixture of distilled water and absolute ethyl alcohol using cotton swabs. Finally, all-liquid inclusions were produced by the same method as described before. Occasionally, naturally occurring brine inclusions were also found in these samples.

Natural salt samples so prepared were essentially single crystallites of rock salt (halite). These samples were expected to have far higher impurity levels than the synthetic single crystals. Due to the inherent weakness of the grain boundaries, it was difficult to machine a polycrystalline sample of natural salt. Also, typical grain size in the original salt specimen was about 1 cm, almost comparable to the desired sample size. Only a limited number of such samples could be prepared, and these contained only one or two large angle grain boundaries.

3.2. OPTICAL HOT STAGE

3.2.1 Description

The experimental set up used to study the migration process of brine inclusions in salt crystals is shown in Fig. 3B. It consists of a transmitted light Nikon Optiphot microscope equipped with a hot stage attachment, a Tiyoda filar eyepiece with goniometer, and four objective lenses with magnifications of 40, 100, 200, and 320.

The hot-stage consists of two copper blocks (A and B) fixed on insulator plate C. The entire assembly can be moved in three principal directions with respect to the objective lens/condenser system. The copper blocks are heated by clamshell electric heaters (D and E) and insulated with 1/4 inch thick Rulon except for small portions at the ends. The salt crystal F is held between the block end faces which have been polished and gold-plated to promote good thermal contact.

The hot-stage attachment maintains the temperature profile in the salt crystal while applying a constant uniaxial stress. The copper block temperatures, measured by Omega platinum resistance temperature detector elements, are held within ± 0.5°C of the preset value by regulating the power to the clamshell heaters by Barber Coleman process controllers. An independent check of the temperatures close to the crystal end faces is made by the means of the thermocouples T1 and T2 in Fig. 3B.

Block B is actually a hollow shell with two sliding copper pieces G and H, the movement of which are controlled by knob I. A Sensotec

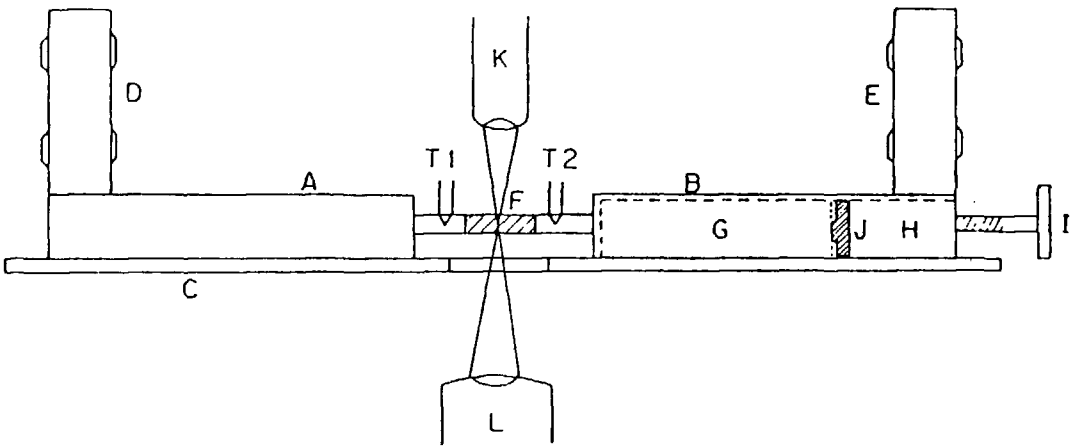

A, B Copper electrodes
C Insulator plate
D, E Clam-shell heaters
F Crystal
G, H Inner copper blocks
I Knob to control load
J Load-cell
K Microscope objective lens
L Microscope condenser
T1, T2 Thermocouples

XBL 809-5916

Fig. 3B. Microscopic hot-state attachment.

miniature load cell J is placed between G and H. The axial load on the crystal is measured by the load cell with its compatible Sensotec amplifier-transducer.

3.2.2 Temperature Profile in the Crystal

The controllers described in section 3.2.1 control the temperatures at the tip of the copper blocks between which the crystal is held. Thermocouples T1 and T2 give an independent measure of these temperatures. However, the exact temperature profile in the crystal determines the thermal environment of the inclusions which are located at different positions in the crystal.

Figure 3C shows the result of computation of this profile for a NaCl crystal under various lateral face conditions when the end faces of the crystal are maintained at 35°C and 105°C, respectively. The figure shows that the maximum difference between the linear profile 1 and profile 4 (where all lateral faces of the crystal are assumed to be cooled by ambient air and heat is also lost by radiation), is about 5°C. This is a difference of about 7 percent at the temperature of 70°C at the center of the crystal. On the other hand, if the crystal is properly insulated from all sides (profile 2), the difference is about 3 percent.

This calculation was tested by measuring the profiles along a NaCl single crystal subjected to a temperature gradient. As shown in Fig. 3D, three holes were drilled in the crystal, and Chromel-Alumel thermocouples were inserted using conducting epoxy. The factory-made thermocouples were of fine size (AWG 30, wire diameter 0.025 cm), and the

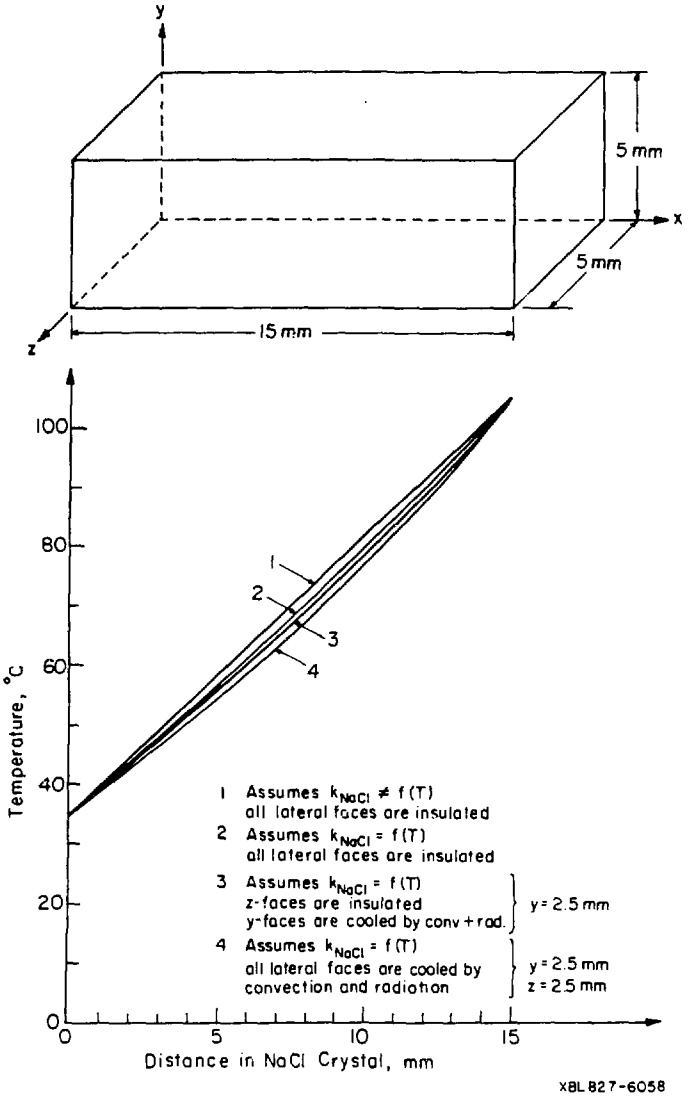

Fig. 3C. Temperature profiles in the salt crystal computed under different conditions.

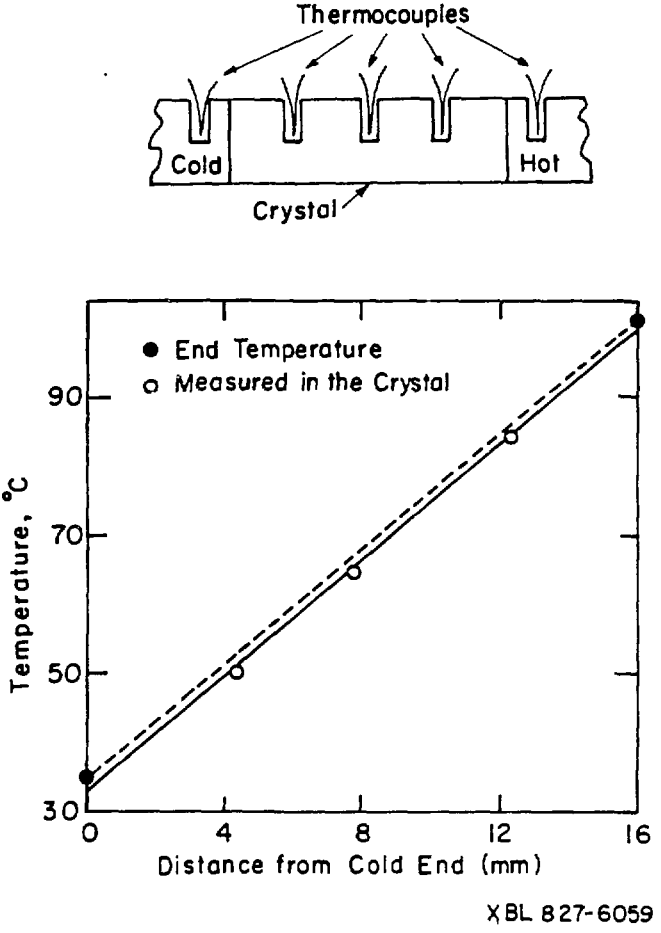

Fig. 3D. Temperature profile measurements in NaCl single crystal.

uniformity of the "bead" or junction assured precise temperature measurements. The measured temperature profile was found to be in excellent agreement with the expected profile 1 as shown in Fig. 3D. No change in the temperature profile was observed when the applied axial load on the crystal was varied over a large range.

Substantiated by the computation and the measurements, the temperature profile in the crystal was assumed to vary linearly along the crystal axis.

3.2.3 Migration Velocity Measurements

A typical observation consists of measuring the inclusion size (thickness L in the direction of the temperature graduation and width W in the transverse direction) and the distance travelled during the time between two successive observations, typically separated by several hours. With the microscopic attachment described previously, these quantities can be measured with an accuracy of ± 1 μm. All side faces of the crystal were kept insulated between measurements. The global temperature of an inclusion at a particular location was obtained by linear interpolation of the crystal end face temperatures.

3.3. DISLOCATION DENSITY IN THE CRYSTAL

The applied axial stress essentially alters the dislocation density in the crystal, which can alter the brine/solid interfacial resistance. Therefore, it was important to estimate this parameter.

There are several standard methods of determining dislocation density in alkali halide crystals. Due to its simplicity and speed, the method of developing etch pits on the surface of the crystal, described

in Ref. [14], was adopted. This method involves treating the surface with selected chemicals etchants. The etched surface develops pits representing emerging dislocations. The etch pits so formed can be observed under an optical microscope. The etch pit technique consists of three basic steps, polishing, etching and rinsing. These are described in detail below.

3.3.1 Polishing

The crystal surface is polished chemically to remove scratches and spots present on the as received crystals to provide a smooth surface for etching. For NaCl and KCl crystals, a 50 percent mixture of deionized water and absolute ethyl alcohol gives good results. This mixture is gently applied to the surface using a cotton tip. The surface is dried in a stream of warm air.

3.3.2 Etching

The etchant contains a concentration of "poison" (usually an inorganic salt) dissolved in a solvent (usually organic). Precise control of poison concentration and etching time (which usually ranges from one second to a couple of minutes) is extremely important. The etchant is applied to the surface by cotton tips or by gently dipping the crystal in a small amount of etchant placed on a petri dish.

For NaCl {100} surfaces, the best results are obtained with a 4 grams/litre solution of $FeCl_3$ in glacial acetic acid with etching time of 30 seconds [15]. For KCl {100} surfaces, a 25 percent solution of $BaBr_2$ in absolute ethyl alcohol gives good results with etching time of about 30 seconds [16].

3.3.3 Rinsing

The etching process is terminated by rinsing the surface with carbon tetrachloride or acetone. The rinsed surface is quickly dried in a stream of warm air.

Figure 3E shows etch pits on a NaCl (100) surface. Each square pit represents an emerging dislocation. The dislocation density is determined by counting the pits on a photomicrograph. A typical NaCl crystal used in this investigation contains about 10^5 dislocations/cm^2.

The etch pit method is very sensitive to the parameters which are sometimes difficult to control (e.g., etching time of the order of a few seconds). Moreover, the dislocations are usually not uniformly distributed but tend to form clusters. Therefore, the results are not always quantitatively conclusive.

Fig. 3E. Dislocation etch pits on the NaCl (100) surface.

XBB 827-6590

CHAPTER 4

THEORY OF THERMOMIGRATION

4.1. ALL-LIQUID INCLUSIONS

4.1.1 Inclusion Velocity

In the section of an all-liquid inclusion shown in Fig. 2A, the symbols C_h^{sat} and C_c^{sat} denote the equilibrium solubilities at the hot and the cold side of the inclusion respectively. Salt transport from the hot to the cold face of the inclusion proceeds through a three-step series mechansim: (1) dissolution at the hot face, (2) molecular and thermal diffusion through the liquid, and (3) crystallization at the cold face.

Supersaturation is required for crystallization to take place and undersaturation is required for dissolution. Both types of departures from interfacial equilibrium are present in a migrating all-liquid inclusion. In Fig. 2A, therefore, $C_h^{sat} > C_h$ and $C_c^{sat} < C_c$ where the subscripts h and c refer to the hot and the cold interfaces, respectively, and the superscript "sat" refers to saturation conditions. The difference $C_h - C_c$ within the liquid brine drives the diffusional transport step. Since the solid is a better conductor of heat than the brine, the temperature gradient across the inclusion ∇T_l is always larger than the applied temperature gradient to the solid, ∇T_∞. The temperature distribution in an all-liquid inclusion is derived in Appendix A.

Because the temperature difference across the inclusion is very small (~0.1°C), the difference in solubilities at the hot and the cold face can be approximated by

$$C_h^{sat} - C_c^{sat} = \frac{dC^{sat}}{dT} L\nabla T_l \tag{4-1}$$

Let the salt flux in each of the three steps previously described be j_s, then the inclusion velocity v is

$$v = \frac{j_s}{\rho_s} \tag{4-2}$$

where ρ_s is the molar density of the solid.

The molecular and thermal diffusional transport in the liquid can be accurately represented by the following equation for the salt flux

$$j_s = \frac{D_l}{L} (C_h - C_c) - \sigma D_l C^{sat} \nabla T_l \tag{4-3}$$

where D_l is the diffusivity of the salt in water, σ is the Soret coefficient, which is taken to be negative when solute moves towards the cold end (this is the case for NaCl and KCl). The fractional undersaturation of the solution at the hot face is defined by

$$\xi_h = \frac{C_h^{sat} - C_h}{C_h^{sat}} \tag{4-4a}$$

and the fractional supersaturation at the cold face is

$$\xi_c = \frac{C_c - C_c^{sat}}{C_c^{sat}} \tag{4-4b}$$

Combining Eqs. (4-1), (4-3), and (4-4) yields

$$j_s = D_l C^{sat} \left[\left(\frac{1}{C^{sat}} \frac{dC^{sat}}{dT} - \sigma \right) \nabla T_l - \frac{\xi_c + \xi_h}{L} \right] \tag{4-5}$$

The sum $\xi_c + \xi_h$ in Eq. (4-5) represents a reduction in the salt flux due to the kinetics of dissolution and crystallization. If interfacial processes do not pose any resistance (by way of requiring undersaturation or supersaturation), $\xi_c + \xi_h = 0$, and combination

of Eqs. (4-2) and (4-5) yields the purely diffusion-controlled inclusion speed

$$v = \frac{D_l C^{sat}}{\rho_s} \left(\frac{1}{C^{sat}} \frac{dC^{sat}}{dT} - \sigma \right) \nabla T_l \qquad (4\text{-}6)$$

As first recognized by Anthony and Cline ([10], [17]), this limiting case is not applicable to a salt-water system. In their treatment $RT(\xi_c + \xi_h)$ was called "kinetic potential". It was found by them to be dependent on inclusion speed, or equivalently, on the salt flux.

4.1.2 Crystal Growth/Dissolution Principles

As evident from Eq. (4-5), the interfacial kinetic processes can contribute substantially to the migration velocity of the inclusion. A brief review of the basic principles and theories of crystal growth/dissolution is appropriate at this point.

Growth occurs when a solute crystal is placed in contact with its supersaturated solution. Conversely, for crystal dissolution to occur, the solid must be in contact with an undersaturated solution. Both the processes are essentially interfacial in nature and involve incorporation into or detachment from the solid of the molecules or atoms of the dissolved solute.

4.1.2.1 Nucleation Growth Theory

The simplest model of crystal growth is that of a perfectly flat solid surface in contact with a supersaturated solution. The solute molecules adsorb onto the crystal surface and tend to form clusters or nuclei of the solute. Thermodynamically, there exists a critical size below which the nuclei will simply redissolve into the solution.

Occassionally, purely by chance, a nucleus of the critical size is formed, which instantly grows into a new layer of the solid. Successive layers are similarly formed and the crystal grows in the direction normal to the surface.

The radius of the critical sized nucleus, r_c, on a perfectly flat crystal surface is thermodynamically given by [18]

$$r_c = \frac{\gamma V_m}{kT\ln(1+\xi)} \tag{4-7}$$

where γ is the interfacial energy, V_m is the volume of a solid molecule, k is the Boltzman Constant, T is the temperature and ξ is the dimensionless supersaturation defined, in terms of actual solute concentration C and saturation concentration C^{sat}, as follows

$$\xi = \frac{C - C^{sat}}{C^{sat}} \tag{4-8}$$

As evident from Eq. (4-7) the requirement of forming a critical-sized nucleus for growth is equivalent to requirement of a critical supersaturation below which no growth occurs. Similarly there should be a critical undersaturation for dissolution to begin.

4.1.2.2 Surface Diffusion Growth Theory

If crystal growth were to take place on a perfectly flat surface by nucleation of critical-sized nuclei, extremely small growth rates are predicted [19]. Calculations show that the nucleation rates in such a case are very small compared to experimentally observed growth rates [19]. The explanation for the discrepancy lies in the imperfect nature of crystal surface. The surface of a real crystal is far from being perfectly flat. As shown in Fig. 4A, it is populated by kinks

(A), ledges or steps (E), vacancies (C), and adsorbed molecules (B and D). The solute molecules constantly adsorb on and desorb from the growing surface. Adsorbed molecules are not tightly bound to the crystal surface and tends to desorb rather quickly. However, kinks have three nearest neighbors and hence atoms attached here are tightly bound to the crystal lattice. Thermodynamically, an extremely small population of kinks exists on the surface and it is a rare event for a solute molecule to hit a kink directly from the solution [19]. However, surface diffusion assists transport of adsorbed molecules to the kink sites where they are likely to get permanantly incorporated into the growing lattice. Frank [20] suggested that emerging screw dislocations on the crystal surface provide a perpetual source of ledges and kinks which act as binding sites (Figure 4B). Therefore, it is likely that dislocations intersecting the inclusions determine the interfacial mass transfer rates.

The scenario of crystal growth from solution is, therefore, as follows. The solute molecules from supersaturated solution constantly adsorb on the crystal surface. Being weakly bound to the surface, adsorbed molecules diffuse on the surface to reach energetically favorable positions (kinks or the ledges created by emerging dislocations). Some adsorbed molecules will, undoubtedly, desorb before they reach the binding sites on these surface defects. However, those which get attached at kinks or ledges are very likely incorporated into the crystal lattice. The kinks are present on the ledges provided by emerging screw dislocations. By adding molecules to the kinks, the dislocation ledge "sweeps" the crystal surface in a

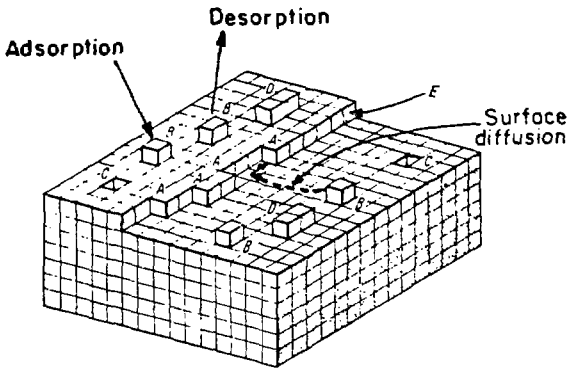

XBL 827-6183

Fig. 4A. (100) Surface of a crystal with simple cubic lattice: A, kinks in the ledge; B, adsorbed molecule; C, vacancies; D, adjacent pair of adsorbed molecules; E, straight ledge (Ref. [19]).

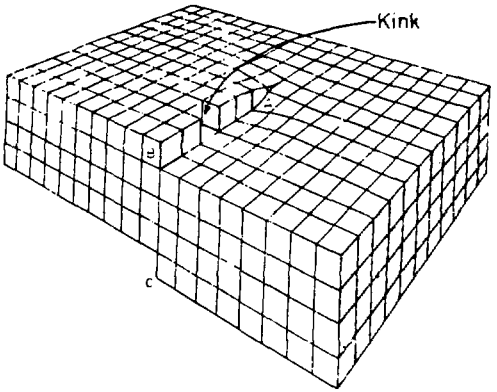

XBL 827-6060

Fig. 4B. A screw dislocation intersecting surface of a simple cubic crystal. The dislocation ledge AB provides energetically favorable sites for crystal growth.

circular motion and winds itself, layer by layer, in the direction normal to the surface. Thus, the crystal grows. For crystal dissolution, a similar scenario, in the reverse sense, takes place.

Burton, Cabrera and Frank developed a surface diffusion crystal growth theory based on the scenario described above. The popularly known BCF Theory is reviewed and rederived in reference [18]. For the present purpose, it is sufficient to state two important results of the theory:

(i) The sweeping ledge motion on the crystal surface, caused by the addition of the solute molecules on the binding sites, depends on parameter r_c as given by Eq. (4-7). The higher the value of r_c, the lower the lateral ledge velocity [18]. The ledge velocity on the crystal surface is directly related to the normal crystal growth rate.

(ii) The final result of this theory in terms of the crystal growth rate normal to surface can be equivalently stated in terms of the net solute flux j_s to the surface as follows

$$j_s = K_1 \xi^2 \tanh \left(\frac{K_2}{\xi} \right) \tag{4-9}$$

where K_1 and K_2 are constants.

Constants K_1 and K_2 depend on temperature, solid density, dislocation density in the solid, the surface diffusion coefficient of the adsorbed molecules, and the average time spent by an adsorbed molecule on the surface. These parameters are generally unknown and therefore only the mathematical form of the ξ-dependence in Eq. (4-9) is useful in a practical sense [18].

In particular, two interesting limiting cases of Eq. (4-9) have application to the theory of thermomigration. At low supersaturation, the values of K_2/ξ is large, the tanh term is ~1, and the growth rate is proportional to ξ^2. On the other hand, at high supersaturations when K_2/ξ is small, the tanh term reduces to its argument, or j_s is proportional to ξ. These are known as non-linear and linear limits of the BCF growth law, respectively. It is noteworthy that unlike nucleation growth theory (Sect. 4.1.2.1), BCF theory does not predict the existence of critical super saturation below which no growth occurs.

4.1.2.3 Impurity Effects

Presence of foreign ions in solution or on the crystal surface can greatly alter crystal growth or dissolution rates. Of particular interest is work of Botsaris [21], who showed that small amounts of lead (i.e. in sub ppm levels) significantly affect the growth rate of the {100} faces of KCl crystals. Usually impurities retard growth, possibly for one of the following reasons [18]:

(i) Impurity adsorption may increase interfacial energy γ. If so, then the theories described earlier predict a growth retardation. As γ increases, the size of the critical nucleus r_c increases which mean a higher critical supersaturation for the growth to proceed according to the nucleation growth theory. For the surface diffusion growth theory, a larger value for r_c means a lower lateral ledge velocity and hence smaller growth rate.

(ii) Immobile impurities adsorbed on the surface hinder the smooth flow of ledges, which is the mechanism of growth. As shown in Fig. 4C, an advancing straight ledge is somehow forced to flow between immobile impurity atoms. The surface diffusion growth theory predicts that the lateral velocity of a curved ledge is lower than that of a straight ledge. In fact, if two impurity atoms are separated by a distance less than $2r_c$, the local ledge curvature becomes so large that the ledge movement completely ceases [18].

Based on this second idea of immobile adsorbed impurities, it can be shown [18,22] that the presence of such impurities leads to a critical supersaturation below which no growth occurs.

4.1.3 Interfacial Kinetics

The principles of crystal growth/dissolution briefly summarized in the previous section will be used here to describe the interfacial kinetics of a migrating all-liquid inclusion.

Because an inclusion is equivalent to a negative crystal, growth steps are automatically provided by the edges of side facets which border the cold face, so that crystallization should be relatively easy. However, steps for dissolution are difficult to form on the hot face [23]. Therefore, the rate limiting interfacial kinetic step is associated with dissolving the hot side of the inclusion [17]. This conclusion is substantiated by the following microscope observation of migrating inclusions; corners between lateral and cold (crystallizing) faces are rounded while the corners between the lateral and hot (dissolving) faces remain sharp. The same phenomena is also evident from the work of Anthony and Cline [10]. The rounded corners at the cold

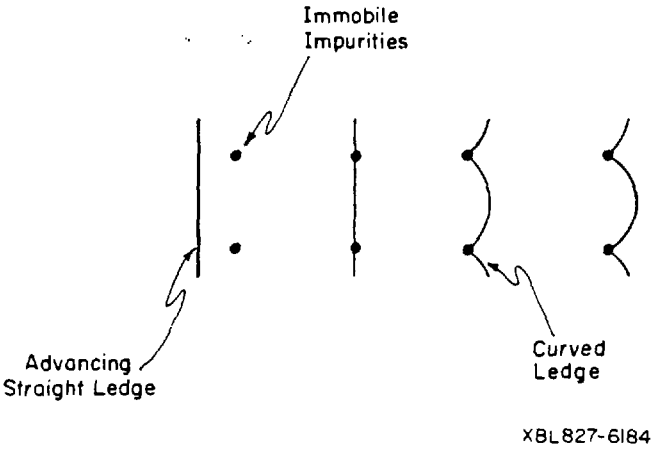

Fig. 4C. Effect of immobile adsorbed impurities on the lateral motion of ledges on the crystal surface.

face of a migrating inclusion provide many ledges or steps for attachment of solute precipitating from solution. This in turn implies that the supersaturation required for crystallization on this face is small. Hence ξ_c in Eq. (4-5) is set equal to zero in the subsequent application of the theory.

Dissolution of a crystal face can be viewed as the reverse of growth and the salt flux at dissolving interface is expressed as:

$$j_s = kf(\xi_h)\, f'(\xi_h, \xi^*) \tag{4-10}$$

where k is an interfacial kinetic coefficient and $f(\xi_h)$ is a function of the fractional undersaturation of liquid in contact with the dissolving face. The product $kf(\xi_h)$ constitutes a phenomenological rate law describing the interfacial kinetics of dissolution of a pure crystal [e.g. Eq. (4-9)] . The function $f'(\xi_h, \xi^*)$ expresses the dependency of the dissolution rate on impurities in the crystal, which results in a critical fractional undersaturation, ξ^* below which no dissolution occurs.

The following functions have been chosen to describe $f(\xi_h)$ and $f'(\xi_h, \xi^*)$:

$$f(\xi_h) = \xi_h^r \tag{4-11a}$$

and

$$f'(\xi_h, \xi^*) = \begin{cases} 1 - \dfrac{\xi^*}{\xi_h} & \text{for} \quad \xi_h > \xi^* \\ 0 & \text{for} \quad \xi_h < \xi^* \end{cases} . \tag{4-11b}$$

Equation (4-11a) encompasses the BCF Theory [Eq. (4-9)], according to

which the exponent r approaches 2 at low undersaturation and tends towards unity at high undersaturation. Equation (4-11b) is justified based on the impurity effects described in section 4.1.2.3.

Equation (4-10) and (4-11) can be combined and used in the migration velocity analysis with the additional specification $r = 1$ (linear model) or $r = 2$ (non-linear model) to conform with the high and low-ξ limits of the BCF Theory.

4.1.3.1 Linear Interface Kinetics

For $r = 1$, the salt flux at the dissolving interface is

$$\begin{aligned} j_s &= k\,(\xi_h - \xi^*) \quad \text{if} \quad \xi_h > \xi^* \\ &= 0 \quad\quad\quad\quad\;\; \text{if} \quad \xi_h < \xi^* \end{aligned} \tag{4-12}$$

Using Eq. (4-12) in Eq. (4-5) together with $\xi_c = 0$ gives the migration velocity

$$v = \frac{1}{\rho_s} \frac{D_1 C^{sat}}{1 + \mathcal{D}} \left[\left(\frac{1}{C^{sat}} \frac{dC^{sat}}{dT} - \sigma \right) \nabla T_1 - \frac{\xi^*}{L} \right] \tag{4-13}$$

where

$$\mathcal{D} = \frac{D_1 C^{sat}}{kL} \tag{4-14}$$

is a dimensionless quantity reflecting relative importance of diffusion in the liquid and interfacial kinetics in the overall transport rate.

This approach is identical to the model formulated by Geguzin et al. [11] and equivalent to one proposed by Anthony and Cline [10], when $\xi_c = 0$. If the kinetic potential K utilized by the latter authors is, as they suggest, a linear function of inclusion speed

$$K = K_0 + \alpha v$$

then coefficients K_0 and α can be identified with the parameters of the linear model as follows

$$K_0 = RT\xi^*$$

and

$$\alpha = RT\rho_s/k \ .$$

Use of these formulae converts the velocity equation derived by Anthony and Cline (Eq. (10) of Ref. [10]) to Eq. (4-13). The parameters K_0 and α are equivalent to the critical departure from saturation and the interfacial transfer coefficient of the linear model.

4.1.3.2 *Nonlinear Interface Kinetics*

For $r = 2$, the salt flux at the dissolving interface is

$$\begin{aligned} j_s &= k\xi_h(\xi_h - \xi^*) \qquad \text{if} \quad \xi_h > \xi^* \\ &= 0 \qquad\qquad\quad \text{if} \quad \xi_h < \xi^* \end{aligned} \tag{4-15}$$

Combining Eq. (4-15) with Eq. (4-5) with $\xi_c = 0$ yield

$$v = \frac{D_1 C^{sat}}{4L\rho_s}\mathcal{D}\left[\left\{\left[\left(1 - \frac{\xi^*}{\mathcal{D}}\right)^2 + \frac{4L\nabla T_1}{\mathcal{D}}\left(\frac{1}{C^{sat}}\frac{dC^{sat}}{dT} - \sigma\right)\right]^{1/2} - 1\right\}^2 - \left(\frac{\xi^*}{\mathcal{D}}\right)^2\right] \tag{4-16}$$

with $\mathcal{D}$ defined by Eq. (4-14).

The limit of kinetic control is obtained for $\mathcal{D}$ sufficiently large and ξ^* small, as

$$v = \frac{k}{\rho_s}\left(\frac{1}{C^{sat}}\frac{dC^{sat}}{dT} - \sigma\right)^2 \left(L\nabla T_1\right)^2 \tag{4-17}$$

while the limit for diffusion control is obtained for small $\mathcal{D}$, in which case Eq. (4-15) reduces to Eq. (4-6). Both these limits are derived in Appendix B.

4.1.3.3 Threshold Temperature Gradient for No Migration

Equations (4-13) and (4-16) predict the migration velocity at a given temperature and inclusion size for the linear and non-linear interface kinetics. Pigford [24] predicted the existence of a threshold temperature gradient below which no migration takes place (i.e. the inclusion remains stationary). At the threshold temperature gradient, the temperature difference across the inclusion is just sufficient to meet the requirement of critical undersaturation for dissolution at the hot interface and critical supersaturation for growth at the cold interface.

Setting the right hand side of Eq. (4-13) and (4-16) equal to zero, the threshold temperature gradient for migration calculated from either of the equations results in

$$\nabla T_{min} = \frac{\xi^*}{-\left(\frac{1}{C^{sat}}\frac{dC^{sat}}{dT} - \sigma\right)} \tag{4-18}$$

which is equivalent to Eq. (29) of Ref. [24].

Similarly for a given temperature and ∇T_∞ (or ∇T_1), there exists a minimum size below which the inclusion becomes immobile. Equation (4-18) can be rewirtten to obtain an expression for this minimum size.

$$L_{min} = \frac{\xi^*}{\left(\frac{1}{C^{cat}}\frac{dC^{cat}}{dT} - \sigma\right)\nabla T_1} . \tag{4-19}$$

Physically the existence of L_{min} means that the inclusion size is so small that, the critical sized nuclei for growth and dissolution [as predicted by Eq. (4-7) for nucleation growth theory, for example] cannot be sustained.

Pigford [24] explained that the existence of the minimum size for migration is responsible for uniformly distributed small sized inclusions in natural salt deposits. During the 200 million-year age under the influence of geothermal gradient, the inclusions would have otherwise migrated towards the bottom of the salt deposits.

4.2. GAS-LIQUID INCLUSIONS

The mechanism of thermomigration of this type of inclusions was discussed in Chapter 2. Referring to Fig. 2B, the following processes must be considered in formulating the inclusion speed in this case:

(i) The diffusion of water vapor in the gas bubble under the driving force of vapor pressure difference between the hot and the cold sides of the bubble. The diffusional flux will depend on gas phase properties such as the diffusion coefficient of water vapor in a given inert gas (helium or air or argon), and the gas phase thermal conductivity.

(ii) The backflow of the liquid driven by the surface tension gradients. Since the surface tension is temperature dependent, a detailed knowledge of temperature distribution in the inclusion is necessary to calculate this backflow. The effect of heat of vaporization of water on the temperature distribution must be accounted for.

(iii) The flux of the dissolved salt in the liquid around the gas bubble. This flux has both diffusional and convective components because salt concentration gradients as well as bulk liquid flow exist in the brine-filled region.

(iv) The interfacial kinetics of dissolution and growth at the cold and the hot brine/solid interfaces, respectively. In principle, these are identical to the interfacial processes at the brine/solid interfaces in all-liquid inclusions which were discussed in the previous section.

It is clear that theoretical modeling of the above processes will require detail calculations of fluid flow, heat, and mass transport in the inclusion. This can not be done analytically for the actual geometry of the inclusion, which is a gas bubble in a cubical brine cavity in an infinite medium of solid. Olander and coworkers [13] have developed an approximate analytical model to determine the velocity of the two-phase fluid inclusions in an imposed thermal gradient. In their analysis, the actual shape of the cavity is approximated by a sphere of radius b with a centrally placed spherical gas bubble of radius a (Figure 4D).

Even with this idealized shape, numerical method is required to solve the concentration distribution of salt in the liquid shell. A further approximation consists of ignoring convective transport in the analysis of the salt-concentration distribution in the liquid shell. This leads to what is called the "approximate solution" [Eq. (115) of Ref. (13)], which provides an explicit and sufficiently accurate equation for the inclusion speed.

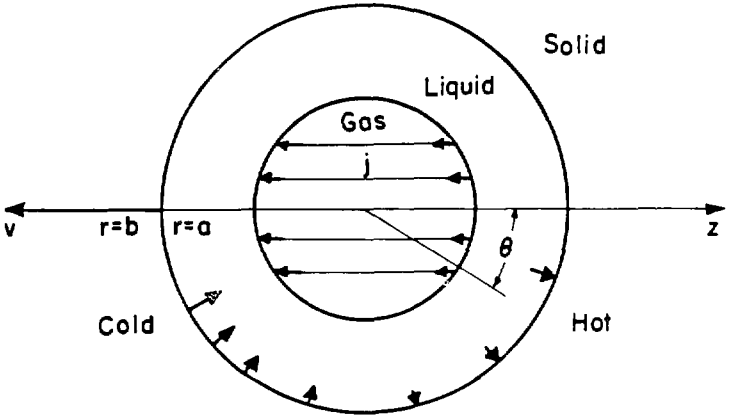

XBL 827-6061

Fig. 4D. Spherical model of a gas liquid inclusion showing the water flux crossing the bubble from hot to cold and the salt deposition or dissolution flux at the solid liquid boundary shown by arrows. (Ref. [13]).

Without going into the details of the analysis of Olander and co-workers [13], it is sufficient here to state that the migration velocity, v, of the inclusion depends on the following parameters:

(1) Global temperature of the inclusion, T at which all the physical property data are calculated.

(2) Applied temperature gradient in solid, ∇T_∞.

(3) The inclusion size, and the volume fraction of gas in the cavity.

(4) The inert gas phase in the bubble (helium or air or argon).

A shorthand representation of Eq. (115) of Ref. [13] is

$$v = f(T, \nabla T_\infty, a, b, \text{gas phase}). \tag{4-20}$$

The actual size of the whole cavity, and the contained gas phase are converted to equivalent spherical sizes given by a and b. The ratio a^3/b^3 give the volume fraction of gas.

CHAPTER 5

INTERFACIAL STABILITY OF MIGRATING ALL-LIQUID INCLUSIONS

5.1. INTRODUCTION

All-liquid inclusions produced in the manner described in Chapter 3 are shaped like square platelets (Figure 3A) with their boundaries conforming to {100}planes of the host single crystal. If L is the thickness of the inclusion and W is the width of one of its square sides, the aspect radio L/W is much less than unity. The thickness L is between 10 and 20 μm, the exact value depending on the temperature and temperature gradient, and the width W is fixed by the volume of liquid contained by the inclusion.

In the present work, it was observed experimentally that certain inclusions showed interface instabilities during migration. Such an instability caused breakdown of an inclusion into two or more smaller but stable inclusions. Anthony and Cline have also reported [25] similar instabilities of brine inclusions in KCl single crystals. However, no rigorous quantitative explanation of such a behavior is available in the literature.

In this chapter a perturbation method is used to analyze interface instabilities of brine filled inclusions in alkali halide single crystals. Using the temperature distribution in the inclusion derived in Appendix A, an approximate theoretical model for the response of a planar solid/solution interface from an arbitrary perturbation is developed. These results are then applied to the interfaces of a migrating inclusion.

According to the analysis of Appendix A the ratio $\nabla T_l / \nabla T_\infty$ decreases from its highest value at the center to unity at the periphery of the inclusion. Because the solubility of salt is temperature dependent, the concentration gradient across the inclusion (which is the driving force for the migration) is also largest at the center. Since the flux of dissolved salt across the inclusion, j_s, depends on the concentration gradient, it should also vary from a maximum value at the center to smaller values at off-axis locations. Alternatively, the flux j_s can be made constant at each point on the inclusion face if the inclusion thickness is highest at the center with continuously decreasing values at off-axis location. This would mean that the inclusion would be roughly spherical in shape. But stable inclusions undoubtedly are square platelet shaped with {100} facets. There are two principal reasons for the observed shape:

(i) The interfacial energy γ is the lowest for {100} planes in KCl and NaCl. Any departure from {100} is energetically unfavorable.

(ii) The interfacial kinetics (discussed in Chapter 4) favors layer by layer growth and dissolution.

Therefore, despite the local variations in concentrations, the stabilizing effects discussed above maintain an inclusion stable with {100} facets and prevent the inclusion from assuming a spherical form. However, these stabilizing effects are not strong enough for inclusions of all sizes. Then the ratio W/L is very large (i.e. for slender inclusions), the gradient amplification factor $\nabla T_l / \nabla T_\infty$ approaches k_s/k_l (which is roughly 7 for NaCl and 10 for KCl). In this limit the

large "gradient effect" overwhelms the stabilizing effects of interfacial kinetics and interfacial energy. As a result, the inclusion breaks down as shown in Fig. 5A.

Figure 5B shows schematically a typical sequence of events during migration which lead to breakdown of an unstable inclusion. The instabilities begin at the corners of the inclusions, where trailing veils first appear. These veils always appear at the interface towards the cold side. The veils lag behind the migrating inclusion for several hours, remaining physically attached to the inclusion. Eventually the veils detach, leaving behind two or more smaller but stable inclusions.

5.2. PERTURBATION METHOD FOR STABILITY ANALYSIS

The application of perturbation method to a growing interface for stability analysis is not a novel subject; the stability of crystal growing from a melt in various geometries (spherical, planar, cylindrical) under mass and heat flows have been analysed by perturbation methods [27], [28], [29], [30]. The subject is adequately reviewed by Sekerka [31] and Delves [32].

A similar perturbation method is used here for a planar crystal growth from solution. There are basic differences between the solidification and solution growth. The former theory has been worked out for temperature gradient zone melting, which refers to the process of solidification at the interface. The solute and solvent are considered to be present on the either side of the interface with a known distribution coefficient. In the case of solution growth, the solid phase is pure solute (no solvent is present in the solid). Other differences

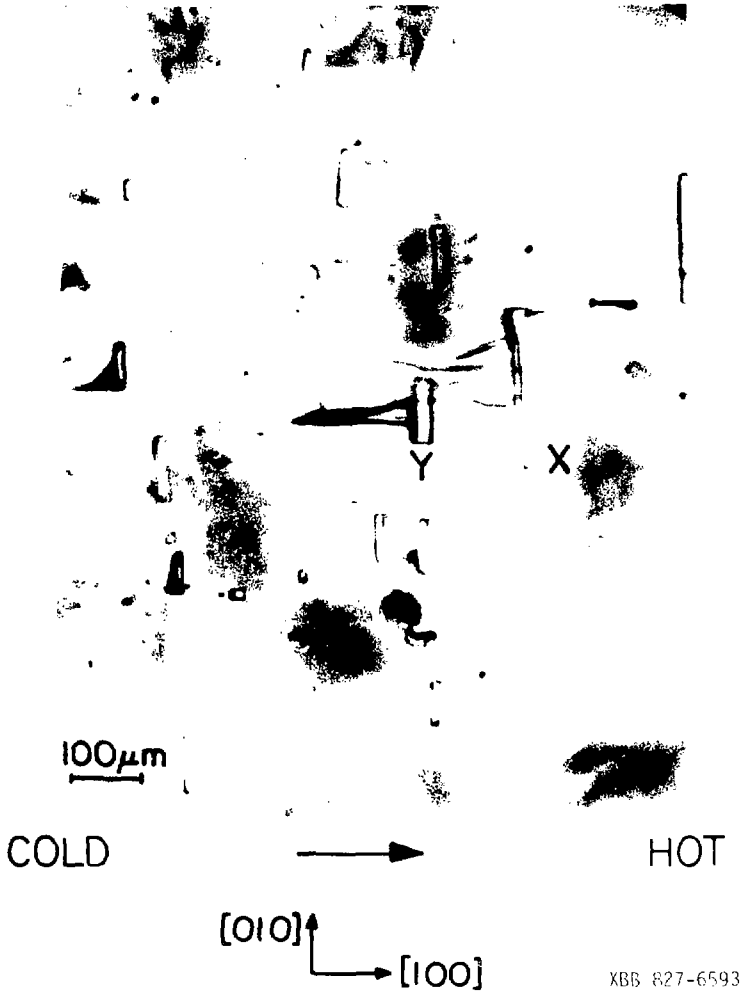

Fig. 5A. Photomicrograph of inclusions showing interfacial instabilities in an applied temperature gradient of 40°C/cm and compressive axial load of ~ 4 MPa. The small sized inclusions are stable with sharp boundaries whereas the inclusions with large W/L ratios have begun to show instabilities at the interface.

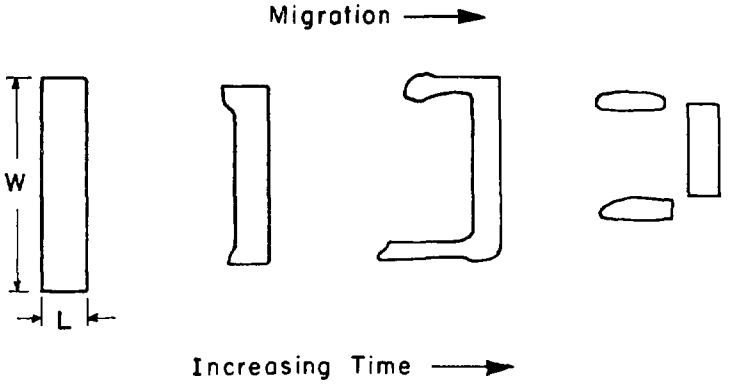

Fig. 5B. A typical sequence of events leading to breakdown of an inclusion.

between the prior studies and the present situation are in the boundary conditions at the interface. Also in the case of solidification, the interfacial velocity is dependent on the latent heat of freezing, whereas the heat of crystallization can be neglected in treating solution growth. (This can be justified by computing appropriate dimensionless numbers for NaCl/brine and KCl/brine cases.) The density difference between solid and liquid are considered here whereas no density change is assumed at the interface in the previous studies.

5.2.1 Temperature and Concentration Fields

Since the migration velocities of the inclusions under consideration are very small (typically 5×10^{-8} cm/s), the velocity terms are neglected in the heat and mass balance equations i.e., the transport equations are assumed to be identical in a fixed frame of reference and in a frame of reference moving with the interface. This assumption results in linear temperature and concentration profiles, which keep the mathematical analysis simple without loss of generality of the conclusions.

5.2.1.1 The Unperturbed Case (superscript "o")

Shown in Fig. 5C is a flat unperturbed planar interface growing from solution. The solid is pure solute crystal with molar density ρ_s.

The temperature and concentration fields in the liquid and the solid are given by:

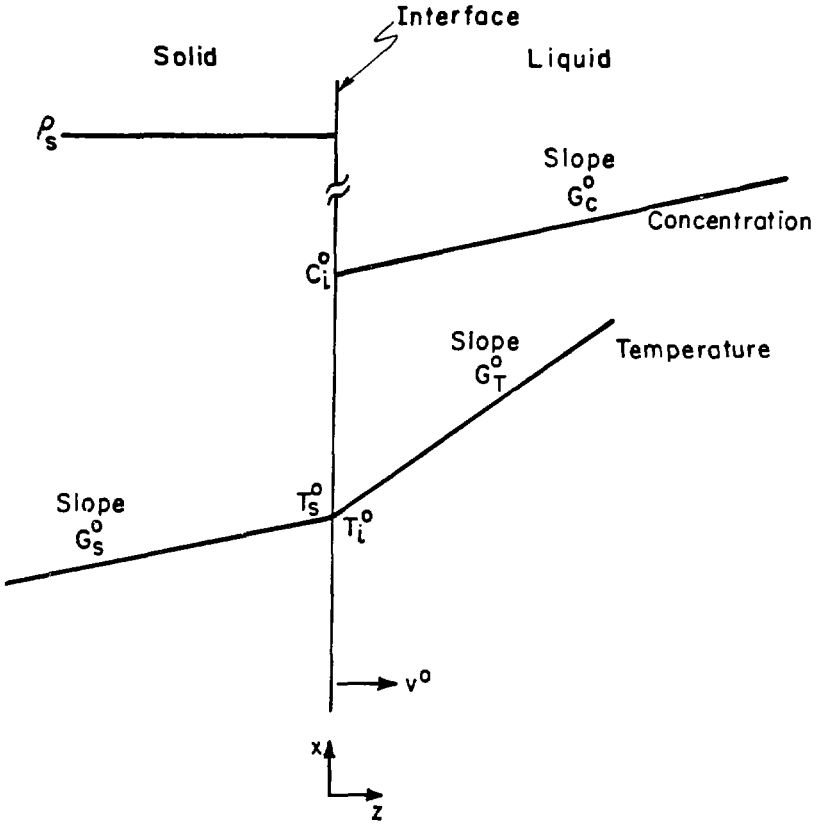

XBL 827-6063

Fig. 5C. Temperature and concentration fields at an unperturbed planar interface under growth conditions. The interface velocity v^o is small.

Liquid ($z > 0$)

$$C^o(z) = C_i^o + G_C^o z \tag{5-1a}$$

$$T^o(z) = T_i^o + G_T^o z \tag{5-1b}$$

where C and T represent concentration and temperature respectively, subscript i refers to interfacial values, and superscript o refers to the unperturbed interface. G_C^o and G_T^o are concentration and temperature gradients in the liquid.

Solid ($z < 0$)

$$C_s^o(z) = \rho_s \qquad \text{(constant)} \tag{5-2a}$$

$$T_s^o(z) = T_i^o + G_s^o z \tag{5-2b}$$

where subscript s refers to the solid and G_s^o is the temperature gradient in the solid. At the interface $z = 0$, continuity of temperature, heat flux, and mass flux gives:

$$T^o(z) = T_s^o(z) \tag{5-3a}$$

$$k_l G_T^o = k_s G_s^o \tag{5-3b}$$

$$D_l G_C^o = v^o(\rho_s - C_i^o) = v^o \rho_s \tag{5-3c}$$

where D_l is the diffusivity of the solute in the liquid.

5.2.1.2 The Perturbed Case

An arbitrary time dependent sinusoidal perturbation with wavelength $\lambda = (2\pi/\omega)$ is given at the interface:

$$z = \phi\,(x,t) = \epsilon\,(\omega,t)\,\sin\,\omega\,x. \tag{5-4}$$

The amplitude of perturbation $\epsilon\,(\omega,t)$ is very small. By solving the heat and mass transport equations in this perturbed case with appropriate boundary conditions, we can find $\dot{\epsilon}/\epsilon$, where $\dot{\epsilon}$ is the time rate of change of amplitude ϵ. If $\dot{\epsilon}/\epsilon$ is negative, the perturbation will decay with time and the interface will be stable. If, on the

other hand, $\dot{\epsilon}/\epsilon$ is positive, the perturbations will grow with time and the interface is said to be unstable.

The conservation equations for the concentration and temperature fields $C(z,x,t)$, $T(z,x,t)$ and $T_s(z,x,t)$ in this case are:

$$\frac{\partial C}{\partial t} = D\left[\frac{\partial^2 C}{\partial x^2} + \frac{\partial^2 C}{\partial z^2}\right] \qquad \text{(for } z \geq 0\text{)} \qquad (5\text{-}5a)$$

$$\frac{\partial T}{\partial t} = D_{th}\left[\frac{\partial^2 T}{\partial x^2} + \frac{\partial^2 T}{\partial z^2}\right] \qquad \text{(for } z \geq 0\text{)} \qquad (5\text{-}5b)$$

$$\frac{\partial T_s}{\partial t} = D^s_{th}\left[\frac{\partial^2 T_s}{\partial x^2} + \frac{\partial^2 T_s}{\partial z^2}\right] \qquad \text{(for } z \leq 0\text{)} \qquad (5\text{-}5c)$$

Note that the convective terms are neglected due to the assumed slow interface velocity. D^S_{th} and D_{th} are thermal diffusivities of the solid and the solution.

In the stability analysis one is interested in the sign of $\dot{\epsilon}/\epsilon$. At $\dot{\epsilon}/\epsilon$ nearly equal to zero, the interface changes shape slowly with time. Hence the time dependent left hand side of Eq. (5-5) can be neglected without loss of generality [32]. The resulting quasi-stationary conservation equations must meet the following conditions:

(i) The solution must reduce to that of the unperturbed case far from the interface. That is,

$$C(z,x) \to C^o(z) \qquad \text{for } z \to \infty \qquad (5\text{-}6a)$$

$$T(z,x) \to T^o(z) \qquad \text{for } z \to \infty \qquad (5\text{-}6b)$$

$$T_s(z,x) \to T^o_s \qquad \text{for } z \to -\infty \qquad (5\text{-}6c)$$

(ii) The interface shape is described by the periodic function $z = \phi(x)$, at which position

$$C_i = C_i^o + a\,\epsilon\,\sin(\omega, x) \tag{5-7a}$$

$$T_i = T_i^o + b\,\epsilon\,\sin(\omega, x) \tag{5-7b}$$

$$T_{s_i} = T_i^o + b'\epsilon\,\sin(\omega, x) \tag{5-7c}$$

where a and b are functions of system properties and remain to be determined.

The solutions to the quasi-stationary forms of Eqs. (5-5) with conditions (5-6) and (5-7) are:

$$C(z,x) = C^o(z) + \epsilon(a - G_C^o)\,\exp(-\omega z)\,\sin(\omega x) \tag{5-8a}$$

$$T(z,x) = T^o(z) + \epsilon(b - G_T^o)\,\exp(-\omega z)\,\sin(\omega x) \tag{5-8b}$$

$$T_s(z,x) = T_s^o(z) + \epsilon(b - G_s^o)\,\exp(+\omega x)\,\sin(\omega x) \tag{5-8c}$$

5.2.2 Determination of the Parameters a and b

The parameters in Eqs. (5-7) are determined by two independent methods. The first is continuity of heat flux and mass flux at the perturbed interface. The second method is based on considerations of interfacial energy and interfacial kinetics.

5.2.2.1 METHOD 1

Mass Flux

$$D_1\left[\frac{\partial C\,(z,x)}{\partial z}\right]_{z=\phi} = v\,(\rho_s - C_i) \approx v\rho_s \tag{5-9}$$

Since ρ_s is much larger than C_i or C_i^o, both C_i and C_i^o can be neglected. From Eqs. (5-8a) and (5-9), with $\exp(-\omega\phi) \approx 1$, for small perturbations

$$D_1 G_C^o - D_1\omega\,\epsilon\,(a - G_C^o)\,\sin\omega x = v\,\rho_s. \tag{5-10}$$

Therefore, since $D_1 G_C^o = \rho_s v^o$ from Eq. (5-3c),

$$-D_1\omega\epsilon\,(a - G_C^o)\,\sin\omega x = \rho_s\,(v - v^o). \tag{5-11}$$

But perturbed interface velocity v can be expressed in terms of the unperturbed interface velocity v^o as

$$v = v^o + d\phi/dt = v^o + \dot{\epsilon} \sin \omega x. \tag{5-12}$$

Substituting Eq. (5-12) into Eq. (5-11)

$$a = G_C^o - \frac{\rho_s}{D_l \omega} \frac{\dot{\epsilon}}{\epsilon} \tag{5-13}$$

Heat Flux

$$k_l \left[\frac{\partial T(z,x)}{\partial z}\right]_{z=\phi} = k_s \left[\frac{\partial T_s(z,x)}{\partial z}\right]_{z=\phi}. \tag{5-14}$$

Using Eqs. (5-8b) and (5-8c), this yields:

$$k_l [G_T^o - \omega \epsilon (b - G_T^o) \exp(-\omega z) \sin\omega x]_{z=\phi}$$
$$= k_s [G_s^o + \omega \epsilon (b - G_s^o) \exp(+\omega z) \sin\omega x]_{z=\phi}$$

Since $k_l G_T^o = k_s G_s^o$ and $\exp(-\omega\phi) = \exp(+\omega\phi) \approx 1$ for small perturbations, we obtain

$$b = \frac{[k_s G_s^o + k_l G_T^o]}{[k_s + k_l]} \tag{5-15}$$

5.2.2.2 METHOD 2

The second method of finding a relation between a and b is similar to that used by Siedensticker [33]. The difference is that Siedensticker considers an interfacial temperature which is different from the "equilibrium" temperature, whereas here it is the interfacial concentration C_i which is different from the saturation concentration C_i^{sat}. This difference is brought about by the interfacial kinetics and interfacial energy (the Gibbs-Thompson Effect). Each of these effects will now be considered separately.

5.2.3 Interfacial Kinetics

According to the theory of crystallization, supersaturation is necessary to initiate crystal growth. Similarly undersaturation is necessary to begin dissolution. As discussed in Chapter 4, according to the nucleation growth theory, this can be attributed to the free energy barrier to form a critical-sized nucleus before growth or dissolution becomes energetically favorable. Whatever the exact mode of interfacial crystallization or dissolution, the difference between the actual and saturation concentrations at the interface (which is the driving force) is related to the interfacial growth or dissolution by an interfacial kinetic law for which a general form is

$$C_i - C_i^{sat} = g(v) \tag{5-16}$$

where g(v) is the function representing the kinetics of the interface attachment or detachment processes. For the unperturbed interface the kinetic law takes the following form

$$C_i^o - C_i^{osat} = g(v^o) \tag{5-17}$$

Because v is close to v^o, g(v) can be approximated by two term Taylor Series

$$g(v) = g(v^o) + \alpha\,(v - v^o) \tag{5-18}$$

where

$$\alpha = \left[\frac{dg}{dv}\right]_{v^o}.$$

Substituting Eqs. (5-16) and (5-17) into (5-18) and then using Eq. (5-12), one obtains

$$C_i - C_i^{sat} = C_i^o - C_i^{osat} + \alpha\dot{\varepsilon} \sin \omega x$$

or,
$$C_i - C_i^o = C_i^{sat} - C_i^{osat} + \alpha\dot{\varepsilon} \sin \omega x \tag{5-19}$$

The concentrations are not continuous at the interface as considered by previous workers. However, the saturation concentration is related to the interfacial temperature. Assuming a linear relation from the phase diagram (which is a good approximation for the NaCl/water and KCl/water systems).

$$T_i^o = m\, C_i^{osat} + \tau \qquad \text{(unperturbed)} \qquad (5\text{-}20a)$$

and

$$T_i = m\, C_i^{sat} + \tau \qquad \text{(perturbed)} \qquad (5\text{-}20b)$$

where m and τ are respectively the slope and the intercept on the phase diagram line. Thus, using Eq. (5-7b)

$$C_i^{sat} - C_i^{osat} = \frac{[T_i - T_i^o]}{m} = \frac{b\epsilon \sin\omega x}{m} \quad .$$

And, using Eq. (5-19)

$$(C_i - C_i^o)_{int\text{-}kin} = \frac{b\epsilon \sin\omega x}{m} + \alpha\, \dot{\epsilon} \sin\omega x \qquad (5\text{-}21)$$

5.2.4 Interfacial Energy

Equation (5-21) gives the difference $(C_i - C_i^o)$ which is attributable to the interfacial kinetic resistance. Now the difference $(C_i - C_i^o)$ due to the interfacial energy will be computed. Since the perturbed interface is curved, capillarity effects must be considered.

Consider a small section of the interface with curvature nearly constant (Figure 5D). Let P_S and P_L be the pressures at the curved interface in solid and liquid, respectively. Similar quantities for the flat unperturbed interface are P_S^o and P_L^o. Since

$$P_S^o = P_L^o.$$

For the perturbed interface

$$P_S - P_L = \gamma \left(\frac{1}{r_x} + \frac{1}{r_y} \right) \qquad (5\text{-}22)$$

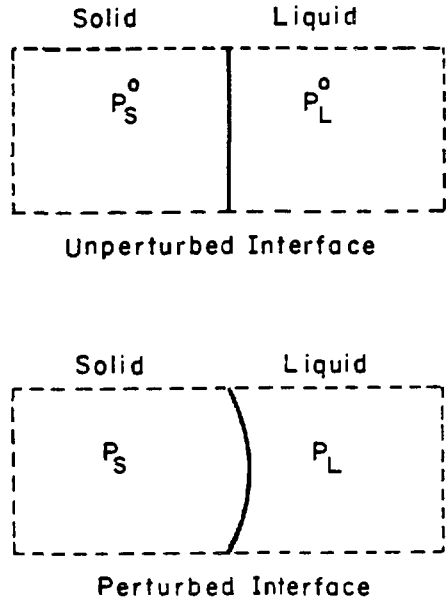

Fig. 5D. Small sections of unperturbed and perturbed interfaces to compute the effect of interfacial energy on the boundary conditions.

where r_x and r_y are two principal radii of curvatures and γ is the surface energy.

But $$\frac{1}{r_y} = 0$$

and $$\frac{1}{r_x} = \frac{\partial^2 \phi}{\partial x^2} = \varepsilon\, \omega^2 \sin \omega x.$$

Therefore, from Eq. (5-22)

$$P_S - P_L = \gamma\, \varepsilon\, \omega^2 \sin \omega x$$

Assuming $P_L = P_L^o$, since the liquid is semi-infinite, yields

$$\Delta P_S = P_S - P_S^o = \gamma\, \varepsilon\, \omega^2 \sin \omega x \tag{5-23}$$

Let $\Delta\mu_s$ and $\Delta\mu_l$ be the changes in the chemical potential of solute in solid and liquid due to the process of perturbing the interface. There

$$\Delta\mu_s = \Delta\mu_l. \tag{5-24}$$

But

$$\Delta\mu_l = k\, T\, \ln \frac{C_i}{C_i^o} \approx k\, T\, \frac{C_i - C_i^o}{C_i^o} \tag{5-25}$$

and $$\Delta\mu_s = \Omega\, \Delta P_s - s\, \Delta T_s \tag{5-26}$$

where Ω is the atomic volume of the solid and s is the entropy. At constant temperature $\Delta T_s = 0$. So from Eqs. (5-23) and (5-26)

$$\Delta\mu_s = \Omega \Delta P_s = \Omega\, \gamma\, \varepsilon\, \omega^2 \sin \omega x \tag{5-27}$$

From Eqs. (5-24), (5-25) and (5-27)

$$k\, T\, \frac{C_i - C_i^o}{C_i^o} = \Omega\, \gamma\, \varepsilon\, \omega^2 \sin \omega x$$

or,

$$(C_i - C_i^o)_{\text{int-enrg}} = \frac{\gamma C_i^o}{kT}\, \Omega\, \varepsilon\, \omega^2 \sin \omega x. \tag{5-28}$$

Adding Eqs. (5-21) and (5-28), the total departure from interfacial equilibrium is given by:

$$C_i - C_i^o = a\,\varepsilon \sin \omega x = \frac{b\varepsilon \sin\omega x}{m} + \dot{\varepsilon} \sin \omega x + \frac{\Omega\gamma C_i^o}{kT}\,\varepsilon\omega^2 \sin \omega x$$

or,
$$a = \frac{b}{m} + \alpha \frac{\dot{\varepsilon}}{\varepsilon} + \frac{\gamma C_i^o}{kT}\,\omega^2 \qquad (5\text{-}29)$$

Substituting a and b from Eqs. (5-13) and (5-15), and solving for $\frac{\dot{\varepsilon}}{\varepsilon}$, one obtains:

$$\frac{\dot{\varepsilon}}{\varepsilon} = \frac{G_C^o - \frac{k_S G_S^o + k_1 G_T^o}{m(k_S + k_1)} - \frac{\Omega\gamma\, C_i^o}{kT}\,\omega^2}{\alpha + \frac{\rho_S}{D_1 \omega}} \qquad (5\text{-}30)$$

The denominator of the right hand side of Eq. (5-30) is always positive, therefore, the sign of $\dot{\varepsilon}/\varepsilon$ is determined by the numerator S, where

$$S = G_C^o - \frac{k_S G_S^o + k_1 G_T^o}{m(k_S + k_1)} - \frac{\Omega\gamma\, C_i^o}{kT}\,\omega^2 \qquad (5\text{-}31)$$

Equation (5-31) is applicable to any solid/solution interface with nonuniform temperature distributions in both phases and a solute concentration gradient in the solution adjacent to the boundary. In the following section, this stability criterion is specialized for the case of an all-liquid inclusion in salt crystals.

5.3. APPLICATION TO MIGRATING INCLUSIONS

With reference to Fig. 2A which shows the temperature and concentration profiles in a section of an all-liquid inclusion:

$$\frac{C_h - C_c}{L} = \frac{\left(C_h^{sat} - \delta C_h\right) - \left(C_c^{sat} + \delta C_c\right)}{L} = \frac{C_h^{sat} - C_c^{sat}}{L} - \frac{\delta C_h + \delta C_c}{L} \tag{5-32}$$

For the cold interface of the inclusion where crystal growth takes place, $\frac{C_h - C_c}{L}$ is approximately equal to the concentration gradient G_c^o used in the previous section. Thus

$$G_c^o = \frac{C_h - C_c}{L} \quad . \tag{5-33}$$

Similarly the temperature gradient within the liquid ∇T_l is approximately equal to $\frac{T_h - T_c}{L}$, where T_c is temperature of a given point on the cold interface and T_h is the temperature of exactly opposite point on the hot interface. Both T_h and T_c are related to the saturation concentrations in adjacent liquid. From phase diagram relation given by Eq. (5-20), therefore

$$\frac{C_h^{sat} - C_c^{sat}}{L} = \frac{T_h - T_c}{mL} = \frac{\nabla T_l}{m} \quad . \tag{5-34}$$

Substituting Eqs. (5-34) and (5-33) into Eq. (5-32) yields

$$G_c^o = \frac{\nabla T_l}{m} - \frac{\delta C_h + \delta C_c}{L} \quad . \tag{5-35}$$

Substituting Eq. (5-35) into Eq. (5-31) yields

$$S = \frac{\nabla T_l}{m} - \frac{k_s G_s^o + k\, G_T^o}{m(k_s + k_l)} - \frac{\delta C_h + \delta C_c}{L} - \left[\frac{\Omega \gamma C_i^o}{kT}\right]\omega^2 \quad . \tag{5-36}$$

The last term in Eq. (5-36) contains ω, the frequency of the sinusoidal perturbation, which is given in terms of the wave length λ by $\omega = \frac{2\pi}{\lambda}$. Because most inclusions begin to break down at corners [25],

a good estimate is $\lambda = W$. With additional assumptions of $G_s^o = \nabla T_\infty$ and $G_T^o = \nabla T_l$, Eq. (5-36) takes the following form

$$S = \frac{\nabla T_l}{m} - \frac{k_s \nabla T_\infty + k_l \nabla T_l}{m(k_s + k_l)} - \frac{\delta C_h + \delta C_c}{L} - \frac{\Omega_\gamma C_i^o}{kT} \left(\frac{2\pi}{W}\right)^2 \quad (5\text{-}37)$$

Using the temperature gradient amplification factor $\mathcal{A} = \nabla T_l / \nabla T_\infty$ at the axis of the inclusion as an approximation in Eq. (5-37), one obtains

$$S = \frac{(\mathcal{A}-1)k_s}{m(k_s + k_l)} \nabla T_\infty - \frac{\delta C_h + \delta C_c}{L} - \frac{\Omega_\gamma C_i^o}{kT} \frac{4\pi^2}{W^2} \quad (5\text{-}38)$$

The first term on the right hand side of Eq. (5-38) is called the "gradient term". The second and third terms are respectively the "interfacial kinetic term" and "interfacial energy term". Since $\mathcal{A} > 1$ (see Appendix A), the gradient term has a positive effect on S and hence is unstabilizing. The interfacial kinetic and energy terms both have negative contributions to S and hence are stabilizing. The same conclusion was previously obtained on qualitative grounds in section 5.1. The condition for stability is $S \leq 0$.

5.4. DISCUSSION

5.4.1 Special Cases

We consider some limiting cases of Eq. (5.38).

Case 1: No Temperature gradient

With the applied gradient $\nabla T_\infty = 0$, Eq. (5-38) indicates that S will always be negative. As intuitively expected, inclusions of all sizes are stable in absence of a temperature gradient.

Case 2: Migration Controlled by Interfacial Kinetics

When migration is entirely controlled by the kinetic resistance at the interface, large supersaturation (δC_c) and undersaturation (δC_h) are needed for the interfacial crystallization and dissolution. In such a case the interfacial kinetic term in Eq. (5-38) is large and negative, and the inclusion will be stable.

Case 3: Purely Diffusion Controlled Migration

This situation is just the opposite of case 2. Neglecting the interfacial kinetic term in Eq. (5-38) results in the following conditions for stability

$$S = \frac{(\mathcal{A}-1)k_s}{m(k_s + k_l)} \nabla T_\infty - \frac{\Omega\gamma C_i^o}{kT} \frac{4\pi^2}{W^2} < 0 \qquad (5\text{-}39)$$

Table 5-1 lists the physical property data in Eq. (5-39) obtained from reference [34]. Substituting values from Table 5-1 in Eq. (5-39) for NaCl/brine at 50°C , the condition for stability in the pure diffusion case reduces to

$$\nabla T_\infty < \frac{8.76 \times 10^{-3}}{(\mathcal{A}-1)\, W^2} . \qquad (5\text{-}40)$$

For a typical inclusion with thickness L of 10 μm and width W of 100 μm, the temperature gradient amplification factor $\mathcal{A}$ is approximately 4, hence the condition for stability reduces to $\nabla T_\infty < 30$°C/cm.

In the range of applied temperature gradients between 0 and 30°C/cm, a typical inclusion of above mentioned size will be stable if its migration is controlled purely by diffusion. However, most inclusions show interfacial resistance controlled migration [9] and hence fall under case 2.

Table 5-1. Physical property data

Property	Units	NaCl/Brine at 50°C	KCl/Brine at T = 40
k_s	$\frac{W}{cm-K}$	5.01×10^{-2}	5.99×10^{-2}
k_l	$\frac{W}{cm-K}$	6.11×10^{-3}	5.81×10^{-3}
$\frac{1}{m} = \frac{dC^{sat}}{dT}$	$\frac{moles}{cm^3 K}$	2.1×10^{-6}	2.54×10^{-5}
$C_i^o \simeq C^{sat}$	$\frac{moles}{cm^3}$	5.45×10^{-3}	4.53×10^{-3}
D_l	$\frac{cm^2}{s}$	2.6×10^{-5}	3.12×10^{-5}
σ	$(°C)^{-1}$	-2×10^{-3}	-1.8×10^{-3}
γ	$\frac{ergs}{cm^2}$	75.65	75.65
ρ_s	$\frac{moles}{cm^3}$	3.68×10^{-2}	2.66×10^{-2}
V_m	$\frac{cm^3}{molecule}$	4.5×10^{-23}	6.24×10^{-23}
kT	$\frac{ergs}{molecule}$	4.46×10^{-14}	4.32×10^{-14}

5.4.2 General Case

In general, inclusions migrate under the combined influence of diffusion and interfacial kinetics. A general condition for stability relating the migration velocity v^o and the applied temperature gradient can be derived as follows:

The flux of dissolved salt as given by Eq. (4-5) can be rewritten as

$$j_s = v^o \rho_s = D_1 \left[\left(\frac{dC^{sat}}{dT} - \sigma C^{sat} \right) \nabla T_1 - \frac{\delta C_c + \delta C_h}{L} \right] \qquad (5\text{-}41)$$

Substituting Eq. (5-41) into Eq. (5-38) with $\nabla T_1 = \mathcal{A} \nabla T_\infty$ and $\frac{1}{m} = \frac{dC^{sat}}{dT}$ yields

$$S = \frac{v^o \rho_s}{D_1} + \frac{(\mathcal{A} - 1)k_s}{m(k_s + k_1)} \nabla T_\infty - \left(\frac{1}{m} - \sigma C^{sat} \right) \mathcal{A} \nabla T_\infty - \left[\frac{\Omega \gamma C_i^o}{kT} \right] \frac{4\pi}{W^2} \qquad (5\text{-}42)$$

Since $C_i^o = C^{sat}$, the above equation reduces to

$$S = \frac{v^o \rho_s}{D_1} - \mathcal{A} \nabla T_\infty \left[\frac{\frac{k_s}{\mathcal{A}} + k_1}{m(k_s + k_1)} - \sigma C^{sat} \right] - \left[\frac{\Omega \gamma C^{sat}}{kT} \right] \frac{4\pi^2}{W^2} \qquad (5\text{-}43)$$

Note that the second and the third terms in the right hand side Eq. (5-43) are always negative (σ is negative for NaCl/brine and KCl/brine). The first term with v^o is positive for the growing cold interface. The condition of stability at the cold interface is obtained by setting $S \leq 0$ in Eq. (5-43), yielding

$$\frac{v^o \rho_s}{D_1} \leq \mathcal{A} \nabla T_\infty \left[\frac{\frac{k_s}{\mathcal{A}} + k_1}{m(k_s + k_1)} - \sigma C^{sat} \right] + \left[\frac{\Omega \gamma C^{sat}}{kT} \right] \frac{4\pi^2}{W^2} \qquad (5\text{-}44)$$

The speed of a migrating inclusion of a given size and aspect ratio in a known gradient must satisfy Eq. (5-44) for stability. If the migration speed is not small enough to meet this condition, the inclusion will break down at the cold interface.

Equation (5-44) was derived for a planar interface growing from solution. At the hot interface of the migrating inclusion, dissolution instead of growth takes place hence v^o is negative. However, the applied gradient ∇T_∞ is also negative when viewed from a coordinate system with its origin at the dissolving surface.

From Eq. (5-44), therefore, the stability condition for the hot interface of the inclusion is:

$$\frac{v^o \rho_s}{D_l} > \mathcal{J} \nabla T_\infty \left[\frac{k_s + k_l}{m(k_s + k_l)} - \sigma C^{sat} \right] - \left[\frac{\Omega \gamma C^{sat}}{kT} \right] \frac{4\pi^2}{W^2} \qquad (5\text{-}45)$$

$$\text{Let} \quad A = \mathcal{J} \left[\frac{k_s + k}{m(k_s + k_l)} - \sigma C^{sat} \right] \cdot \frac{D_l}{\rho_s} \qquad (5\text{-}46)$$

$$\text{and} \quad B = \left[\frac{\Omega \gamma C^{sat}}{kT} \right] \left(\frac{4\pi^2}{W^2} \right) \cdot \frac{D_l}{\rho_s} \qquad (5\text{-}47)$$

Then Eqs. (5-44) and (5-45) give the following conditions for stability

at the Cold Interface:

$$v^o \leq A \nabla T_\infty + B \qquad (5\text{-}48a)$$

at the Hot Interface

$$v^o \geq A \nabla T_\infty - B \qquad (5\text{-}48b)$$

Equations (5-48) are general stability conditions for an all-liquid inclusion in a crystal supporting an external temperature gradient.

5.4.3 Comparison with Experimental Data

Figure 5E schematically shows a sketch of Eqs. (5-48) with the regions of stability for an inclusion with specific values of L and W. The stability region bound by straight lines in Fig. 5E is valid only for constant values of L and W. In practice, however, a given inclusion flattens in the direction of applied temperature gradient as the gradient is increased (i.e. with an increase in ∇T_∞, L decreases and W increases keeping the inclusion volume W^2L constant). Since parameters A and B defined in Eqs. (5-46) and (5-47) depend on L and W, the slope and the intercept of the stability lines on Fig. 5E should actually vary with ∇T_∞. Therefore the stability region is, in fact, determined by the complex inter-relation between v^o, ∇T_∞, L, and W for a given inclusion.

Table 5-2 summarizes the values of parameters A and B at a specified temperature for NaCl and KCl as the inclusion width W is varied keeping the thickness L constant at 10 μm. The physical property data of Table 5-1 are used to compute A and B. For an inclusion migrating with a velocity v^o under the combined influence of diffusion and interfacial kinetics in a crystal supporting a temperature gradient ∇T_∞, the experimental values of L and W, together with the physical property data at the temperature of the inclusion, determine whether or not the condition stated in Eqs. (5-48) are met.

A simpler stability criterion exists for inclusion migrating under purely diffusion control. For the cold interface of the inclusion, this condition is given by Eq. (5-39), which can be rewritten as

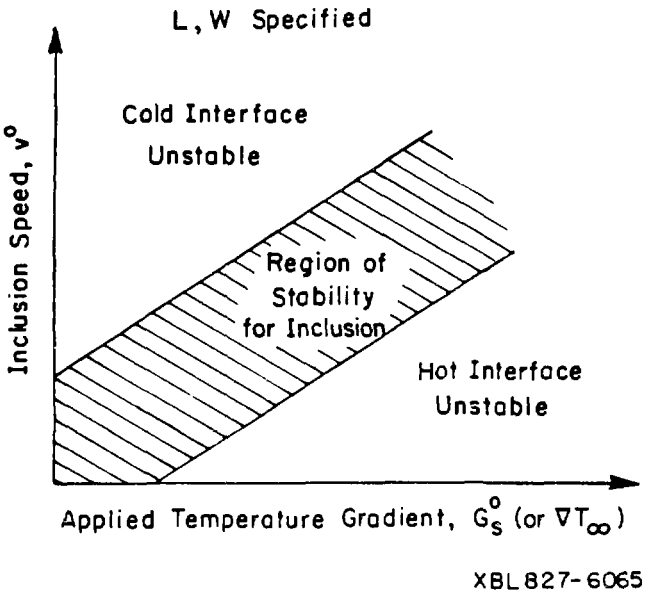

Fig. 5E. Schematic representation of the region of stability for an inclusion with specific values of L and W migrating under the combined influence of diffusion and interfacial kinetics.

Table 5.2. Stability parameters for inclusions in NaCl and KCl (Inclusion thickness L = 10 μm)

Inclusion Width, W μm	NaCl T = 50°C		KCl T = 40°C	
	A [Eq. (5-46)] (10^8cm^2/°C-s)	B [Eq. (5-47)] (10^8cm/s)	A [Eq. (5-46)] (10^8cm^2/°C-s)	B [Eq. (5-47)] (10^8cm/s)
10	1.23	1160.0	4.44	23600.0
25	1.70	186.0	5.20	3770.0
50	2.42	46.4	6.47	944.0
100	3.32	11.6	8.16	236.0
500	5.40	0.5	12.42	9.4
1000	5.88	0.1	13.67	2.3
∞	6.52	0.0	15.25	0.0

$$\nabla T_\infty < \left[\frac{\Omega\gamma C^{sat}}{kT}\right]\left(\frac{(k_s + k_l)}{k_s\,(1/m)}\right)\frac{4\pi^2}{(\mathcal{A}-1)\,W^2} \qquad (5\text{-}40)$$

Experimentally inclusions can be forced to migrate with up to 80 percent of the theoretically calculated diffusion controlled velocities by increasing the axial load on the solid crystal (see section 3.3). To test the condition in Eq. (5-40), four inclusions (F,G,H,I) with sharp boundaries were followed in a KCl crystal supporting an external temperature gradient and axial load of 4 MPa. As the temperature gradient ∇T_∞ was varied, the inclusion size (L and W) was carefully noted at regular intervals. The results are shown in Fig. 5F. Most experimental points are well within the stable region.

The inclusions shown in Fig. 5A are migrating in a KCl single crystal to which an external temperature gradient of 40°C/cm and axial compressive load of ~ 4MPa is imposed. These inclusions are expected to migrate with up to 80 percent of the theoretical diffusion controlled velocities. The inclusions marked X and Y on Fig. 5A are clearly unstable by virtue of having long trailing veils of liquid which are separating away from the cold interface. Some other inclusions also show similar veils of instability. Such inclusions are within the unstable region of Fig. 5F.

On the other hand, some inclusions of approximately same size as that of X and Y (which will also fall in the unstable region of Fig. 5F) do not show the trailing veils of instability. These apparently stable inclusions may in fact be unstable inclusions whose veils may not have grown sufficiently long, since the onset of the instability, to be clearly visible at the magnification used in the photomicrograph

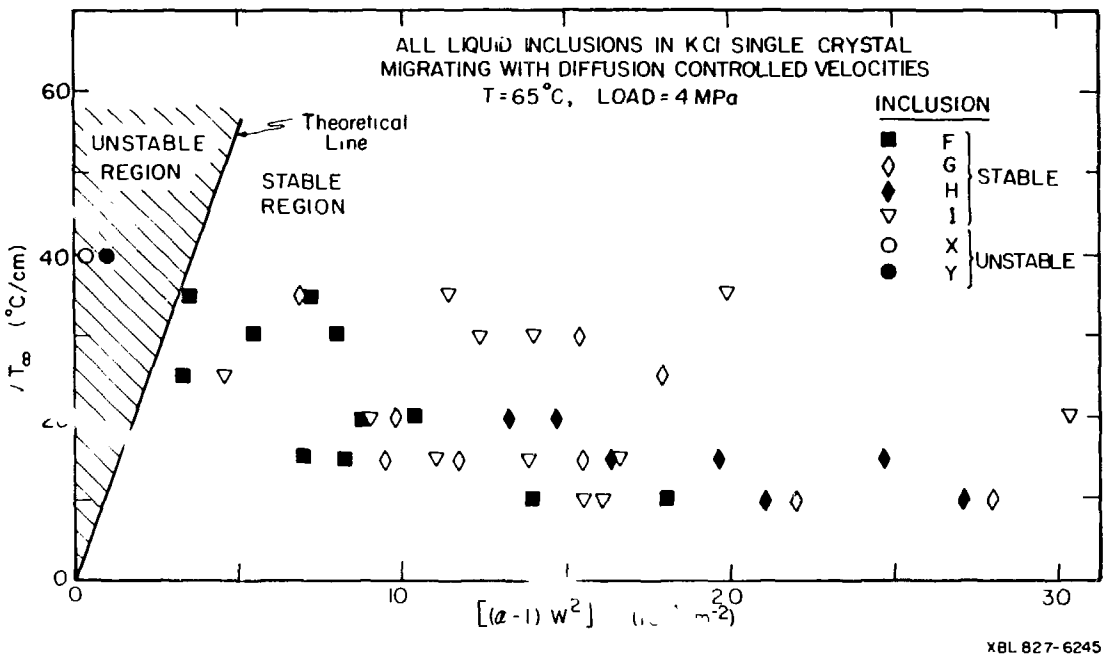

Fig. 5F. Experimental data for several stable and unstabled inclusions migrating with diffusion controlled velocities in a KCl single crystal.

of Fig. 5A. In other words, the presence of trailing veils of liquid is a sufficient but not a necessary condition of interfacial instability.

The theoretical line in Fig. 5F is computed for an extreme limit of purely diffusion controlled migration. In practice, however, most inclusions exhibit certain interfacial mass transfer resistance even when high axial compressive loads are applied to the crystal. It will be further elaborated in Chapter 6 that two inclusions of the same size under otherwise identical conditions often have different values of interfacial parameters (and hence different stability criteria) due to stochastic nature of interaction between dislocations and migrating inclusions.

5.4.4 Comparison with the Work of Anthony and Cline

The approach used in the present work is more accurate compared to the stability condition previously proposed by Anthony and Cline [25]. Based on experimental data, Anthony and Cline [25] proposed a maximum value of 9.4×10^{-8} $cm^2/sec^{\circ}C$ for the ratio $v/\nabla T_{\infty}$, above which all inclusions become unstable. In their data, temperature does not appear to be held constant for different inclusions. Their data obtained for several inclusions in a KCl single crystal in a temperature gradient inherently imply that the inclusions were at different temperatures by virtue of being at different locations in the crystal. Moreover, the inclusion size and shape is unaccounted for in their work.

It is clear from Eqs. (5-48) that both temperature and inclusion shape and size are very important parameters in stability analyses.

Although Anthony and Cline data [25] are abundant, it is not possible to make any meaningful comparison of their data to the present work.

5.5. SUMMARY

An approximate analytical approach is used to explain the interfacial instability of all-liquid inclusions in alkali halide single crystals supporting an external temperature gradient. It is clear that the interfacial kinetics is a strong stabilizing force and that inclusions migrating with interfacial kinetic control are always stable. For a diffusion controlled migration, the inclusions are unstable above a temperature gradient which is inversely proportional to the square of the inclusion width W. For a mixed diffusion-interfacial kinetics controlled migration, stability conditions are separately derived for the cold and the hot interfaces of the inclusion.

CHAPTER 6

RESULTS AND DISCUSSIONS

6.1 ALL LIQUID INCLUSIONS

6.1.1 Potassium Chloride Single Crystals

6.1.1.1 Solid Unstressed

According to the BCF theory discussed in Chapter 4, the rate of removal of solid from the hot face of an inclusion depends on the presence of dislocations intersecting this surface. Dissolution steps are provided by screw dislocation ledges on the surface. Assuming a dislocation density of 10^5 cm^{-2}, as estimated by etching method described in Chapter 3, and an inclusion 50 μm wide, the average number of dislocations intersecting the dissolving face is 2.5. Therefore, substantial differences in the coefficient k of Eq. (4-10) can be expected from one inclusion to another due solely to the statistical variations of this number. Changes in crystal growth rate with size (size-dependent growth) and variations of growth rate for a given size (growth dispersion) are well-documented phenomena [35] which support the above argument.

In addition, the dissolution rate will in general be different for two inclusions which are intersected by the same number of dislocations on the hot face. The temperature gradient, and hence the temperature, vary considerably over the face perpendicular to the thermal gradient (see Appendix A). Hence, a dislocation near the axis will be a more prolific source of dissolution steps than one near the edge of the inclusion.

Thus, the number and the location of the dislocations intersecting the hot face of the inclusions are believed to be responsible for the average velocity under specified conditions as well as the dispersion about this average value. The additional experimental results described below support this general interpretation of inclusion migration.

Figure 6A shows the migration velocity of a single inclusion in KCl which was followed for 72 h. Periodic measurements of the position of the inclusion allowed the average speed between successive observations to be determined. These average velocities are shown as the horizontal line segments on Fig. 6A. The long segments indicate a large interval between measurements; they do not imply that the inclusion velocity was constant over this interval. The velocity of the inclusion followed in this test changed by a factor of four, from a minimum value of ~8 μm/h to a maximum of ~32 μm/h. The change was fairly smooth--the velocity tended to increase or decrease continuously for long periods of time. This behavior is most easily interpreted in terms of the dynamic interaction between the inclusion and dislocations in the crystal.

The dislocations in the crystal are modeled as lines which intersect the hot face of the inclusion at random off-axis locations with random angles from the normal to the surface. The interfacial kinetic coefficient depends on the number of dislocations which intersect the hot side of the inclusion as well as their off-axis locations, which determine the application ∇T_1 (see Fig. A1). Since ∇T_1 is greatest at the centre of the inclusion and $\nabla T_\infty = \nabla T_1$ at the inclusion boundary

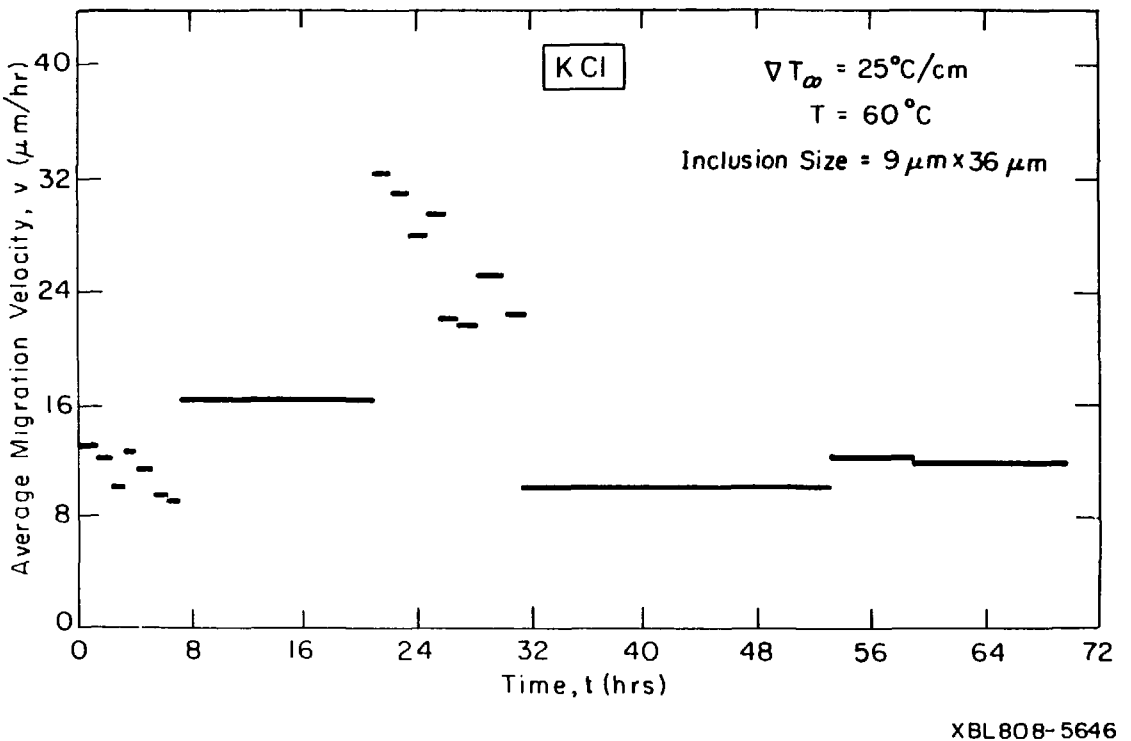

XBL808-5646

Fig. 6A. Migration velocity of an inclusion in KCl as a function of time.

(Appendix A), there is no fixed value of ∇T_1 for a given inclusion which may encounter a dislocation intersection whose position on the hot face continuously varies as it migrates.

In general, a dislocation does not intersect the hot face at 90°, so that as the inclusion moves, the lateral position of the intersection changes. This causes the inclusion to speed up (if the intersection approaches the axis) or to slow down (if the intersection moves towards the edges). In addition, the inclusion can pick up or lose dislocations as it moves, which would result in abrupt velocity changes. This type of intersection is consistent with the sizable variations of the speed of a single inclusion (Fig. 6A). The model also provides an explanation for the large scatter in the velocities of different inclusions measured under the same nominal conditions.

The pattern shown in Fig. 6A can be rationalized in the manner shown schematically in Fig. 6B. At time zero, imagine that the hot face of the inclusion is intersected by a single dislocation (No. 1) close to the centre of the face. In general, the dislocation does not intersect the surface at 90°, so that as the inclusion moves, the intersection point moves further off axis. At off-axis positions, ∇T_1 is less than it is close to the axis, and hence inclusion slows down. Somewhere between 8 and 20 hours the inclusion picks up another dislocation designated as No. 2 in Figure 6B. The three dislocation intersections with the desolving face result in a several-fold increase in the inclusion velocity. As the intersection of No. 2 dislocation with the hot face in off-axis, the inclusion begins to slow down. The inclusion followed in Fig. 6A seems to be capable of sustaining a minimum

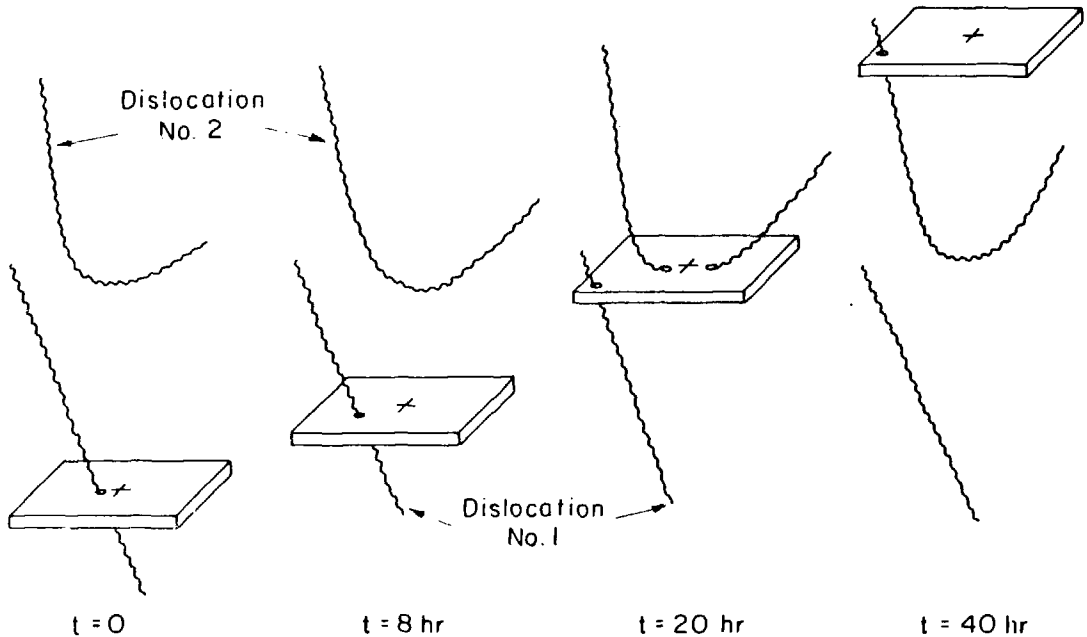

XBL 8010-6068

Fig. 6B. Schematic sketch of dislocations in the crystal as they encounter migrating inclusions.

speed of ~8 μm/hr, which may represent the velocity in absence of any dislocation intersection with dissolving face.

Although the scenario described above is only illustrative, it is clear that the dislocation hypothesis is quite consistent with the stochastic nature of the measured inclusion speeds seen in Fig. 6A. Essentially the same ideas were also used by Lemaire and Bowen [36] to explain pore migration in KCl due to a temperature gradient.

Tests were made to distinguish between control of the migration velocity by liquid diffusion and by interfacial kinetics. In these tests, several inclusions were selected and the applied temperature gradient ∇T_∞ was varied while keeping the temperature in the vicinity of the inclusions constant. Each time ∇T_∞ was changed, the inclusions changed shape. In general, large gradients ∇T_∞ are associated with small inclusion thickness L. This shape change, and the reverse process of shape relaxation, have been analyzed by Olander and coworkers [9]. Figure 6C shows the variation in inclusion size with applied temperature gradient according to Eq. (A12) of Ref. [9].

For interface kinetic control, Eqs. (4-15) and (4-17) indicate that the velocity should depend upon the product $L\nabla T_1$ raised to some power other than one. For each ∇T_∞ and inclusion shape, the centerline ∇T_1 was calculated by the method described in Appendix A. Figure 6D shows the velocities of five inclusions plotted in this manner. The slopes on the log-log plots range from 2.0 to 3.4. Figure 6D also shows the diffusion-controlled limits calculated from Eq. (4-67) for the two temp-

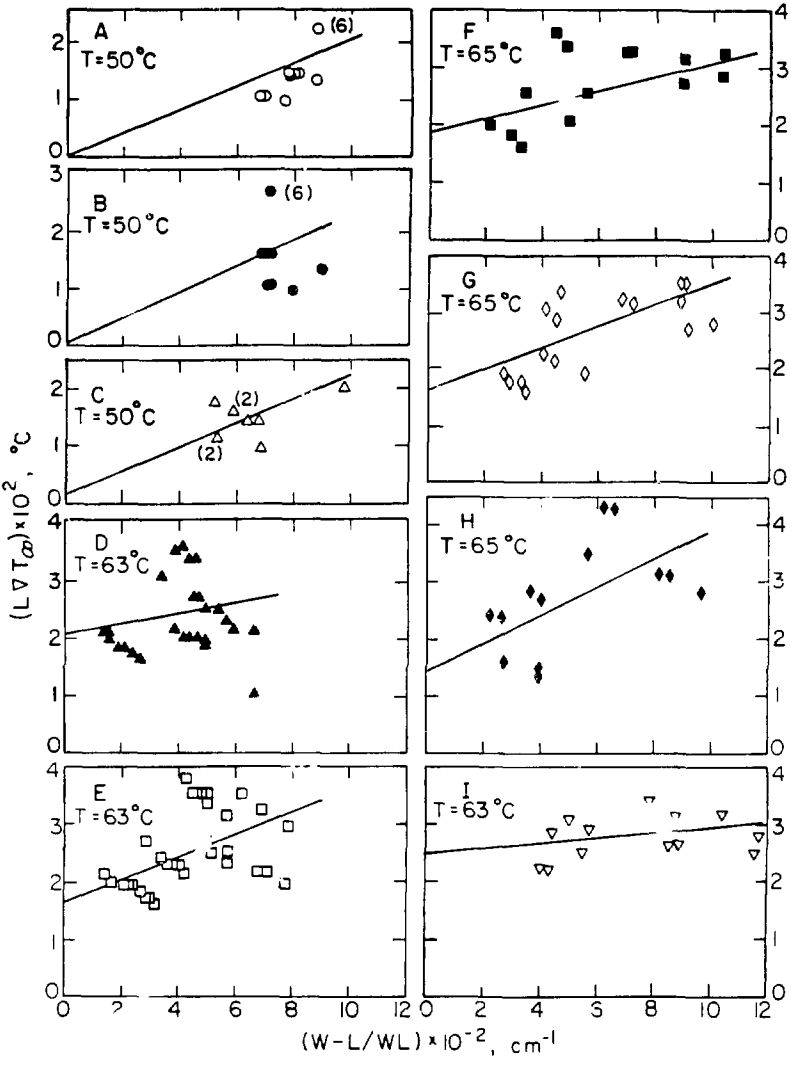

Fig. 6C. The variation in inclusion size with applied temperature gradient fitted to Eq. (A12) of Ref. [9]. The inclusion volume is $L_o^3 = W^2L$.

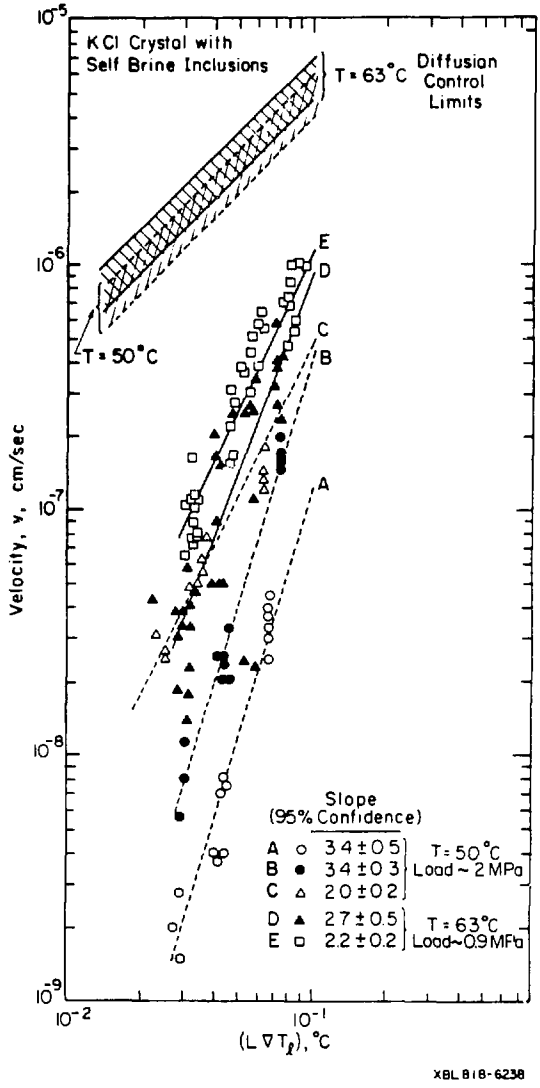

Fig. 6D. Variation of migration velocity of five inclusions in KCl with the applied temperature gradients. The lines represent best fit curve from the theory [Eq. (4-16)].

eratures with the required physical property data taken from Ref. [34]. The upper and lower limits correspond to the lowest and highest values of inclusion thickness ($\sim 9\ \mu m \leq L \leq \sim 13\ \mu m$) observed experimentally as the temperature gradient was varied. The observed velocities for all five inclusions are one to three orders of magnitude lower than the diffusion-controlled limits, indicating that interfacial kinetics is rate-limiting. The slopes close to 2.0 are in accord with the low-ξ limit of the BCF model [Eq. (4-17)]. The higher values of exponents are attributed to the impurity effects which, as discussed earlier, is manifest as the critical undersaturation parameters ξ^*. As ξ^* increases, Eq. (4-16) predicts that v should increase with $L\nabla T_l$ more rapidly than $(L\nabla T_l)^2$. This is proved mathematically in Appendix B.

Velocity calculations require specification of the temperature gradient ∇T_l. Previous work of Anthony and Cline, [10] and Geguzin et al. [11] as well as the analysis needed for preparation of Fig. 6D, utilized the temperature gradient along the inclusion axis, which may be several times larger than ∇T_∞. When the inclusion velocity is controlled by interface kinetics, this choice is valid only if the defect responsible for solid dissolution is located at the center of the dissolving face. However, the dislocation intersections are randomly distributed over the hot face of the inclusion, and for each intersection, the local ∇T_l is the appropriate one. No theory of inclusion migration provides guidance on the choice of ∇T_l. Yet because the inclusion retains {100} faces perpendicular to the applied temperature gradient, it is evident that only a single value of ∇T_l controls the

migration speed. If the kinetics of dissolution, diffusion, and crystallization followed the local value of ∇T_1, the inclusion would adopt a spherical shape, as discussed in Chapter 5. Obviously the great stability of the {100} faces prevents such deformation. As the reverse of crystal growth, dissolution proceeds by removal of molecules from surface steps which as a result move across the surface to the inclusion edges [37]. This process retains a flat dissolving surface except for pyramidal depressions centered on each dislocation intersection. The use of the center-line ∇T_1 in data analysis is arbitrary, but a choice is unavoidable.

6.1.1.2 Effect of stress

Figure 6E shows the effect of increasing the axial load on the crystal by several fold during the migration process. At the time of the stress increase, the migration velocities of the two inclusions being followed jumped abruptly and continued to increase with time under the higher load. This behavior is attributed to the activation of dislocation sources in the crystal by the increase in load an their continued movement by creep at the high load. As a result of the increased dislocation motion, more dislocation intersections with the inclusions occurred, thereby decreasing the resistance to dissolution of the hot face for the prevailing undersaturation and increasing the inclusion speeds. The velocities do not return to their initial values upon removal of the load, so the effect is not elastic.

To observe the effect of axial load on the migration speed, another set of experiments was performed. First, the velocities of four

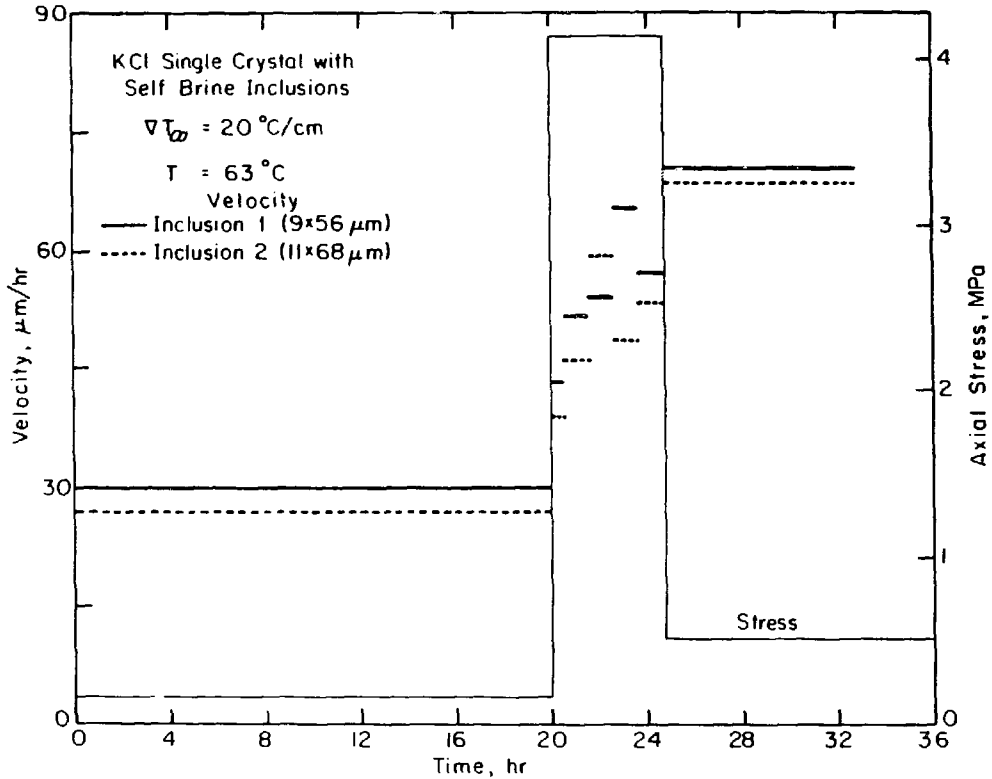

Fig. 6E. Effect of increasing the mechanical load on a salt crystal containing inclusions migrating in a temperature gradient.

X8L818-6236

inclusions (F, G, H, and I) were followed as the applied temperature gradient was varied at constant temperature and low axial load. The same four inclusions were then monitored at axial loads of about 4 MPa. The results are plotted in Fig. 6F for both conditions. As expected from the dislocation arguments presented here, the velocities are higher at the higher load, attaining from 60 percent to 80 percent of the diffusion-controlled limits. In addition, the velocities are proportional to $(L\nabla T_1)$ at high axial load and to $(L\nabla T_1)^2$ at low axial load. This load response of the inclusion velocities is in excellent agreement with the model. At low loads the dislocation density in crystal is small and there are few dislocation intersections with the dissolving face of the inclusions. At high loads the dislocation density is increased by deformation and more dislocations intersect the inclusion, making dissolution of the hot face easier. As a result of the reduced interfacial kinetic resistance, the inclusions move at nearly the liquid diffusion-controlled rate.

6.1.1.3 Evaluation of Interfacial Kinetic Parameters

The experimental aspect ratio data fitted to Eq. (A12) of Ref. [9] are shown in Fig. 6C for nine inclusions (A-I). The interfacial energy γ and the critical undersaturation ξ^* obtained from the fitting are listed in Table 6-1. Similarly by fitting the migration speed data in Figs. 6D and 6F to Eq. (4-16), the value obtained for interfacial kinetic coefficient k and critical undersaturation ξ^* are also listed in Table 6-1. The interfacial energy γ is the same orders of magnitude as the values reported by Anthony and Cline [10], and Geguzin et al. [11].

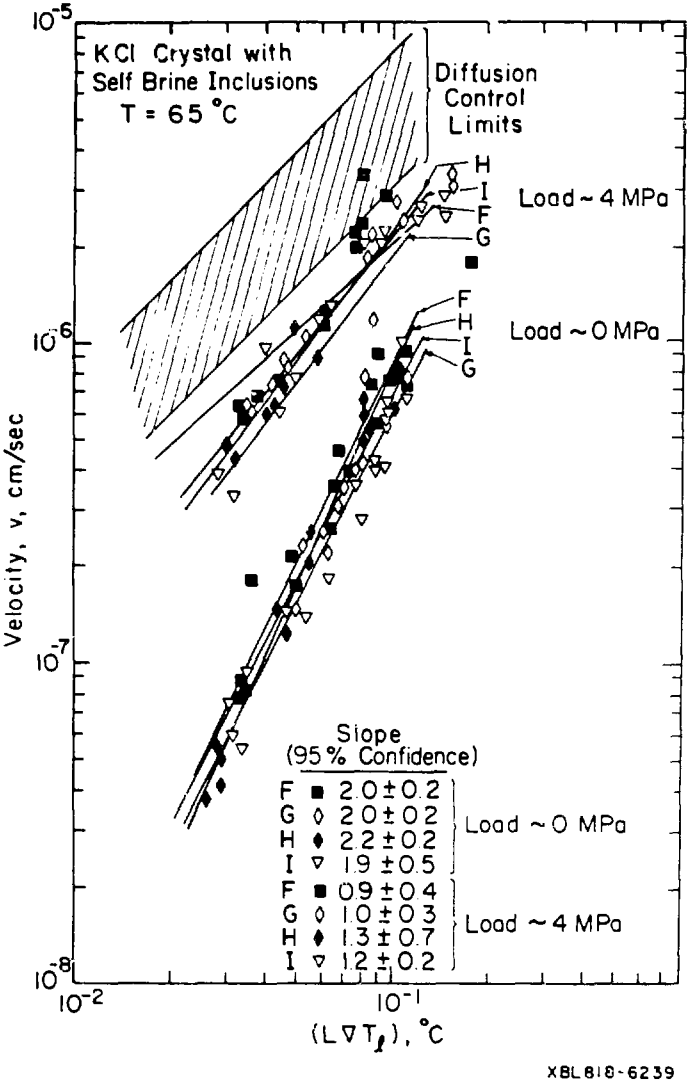

XBL818-6239

Fig. 6F. Effect of applied axial load on the inclusion migration speeds. The lines represent the best fit curves from the theory [Eq. (4-16)].

Table 6-1. Interfacial parameters of KCl (self brine).

Inclusion No.	Temp. °C	(100) Surface energy, ergs/cm^2 from Eq. (A12) of Ref. [9]	Critical Undersaturation, $\xi^* \times 10^5$ From Eq. (A12)	From Eq. (4-16)	Kinetic Coefficient k (mol/cm^2 - s)x 10^2 From Eq. (4-16)[b]
A	50	38	~0	21	1
B	50	49	0.4	22	3
C	50	39	0.7	1	3
D	63	15	9	10	9
E	63	30	7	9	18
F	65	20	7	8	7(370)[a]
G	65	28	7	~0	6(270)
H	65	36	6	3	8(100)
I	65	6	10	~0	6 (72)

[a]Values in parentheses refer to crystals stressed to 4 MPa; all others refer to low-load experiments.

[b]v_1 taken to be the centerline value.

The critical undersaturation ranges from 10^{-5} to 10^{-4}, but there are some inconsistencies between the values deduced from inclusion aspect ratios using Eq. (A12) of Ref. [9] and from the velocity measurements by Eq. (4-16). The interfacial kinetic coefficient with no load on the crystal are between 10^{-2} and 10^{-1} mol/cm^{2}s. The substantial variability of these results is a reflection of the stochastic nature of the dislocation intersection with the dissolving face of the inclusion as discussed earlier.

The numbers in the parenthesis in the last column of Table 6-1 show the best fit values of k for inclusions F-I after the load on the crystal had been increased to ~ 4 MPa. The very large interfacial coefficients imply diffusion control of the migration process.

6.1.2 Sodium Chloride Single Crystal

6.1.2.1 Self Brine Inclusions

Balooch and Olander [38] noted that the data of Anthony and Cline [10], and Geguzin et al. [11] are in single crystals of KCl, whereas from the point of view of applications in salt repository, it is more appropriate to obtain data in NaCl single crystals. Their data suggest a rapid increase in migration speed with increase in inclusion size W. Assuming interfacial kinetic control, the increase in migration speed with width W can arise from a larger temperature gradient amplification factor $\mathcal{A}$ (Fig. A1) and from the fact that the large inclusions should intersect more dislocations than smaller ones, which in turn, increase the dissolution rate.

In Fig. 6G data of Anthony and Cline [10], and Geguzin et al. [11] in KCl are compared with those of Balooch and Olander [38] in NaCl.

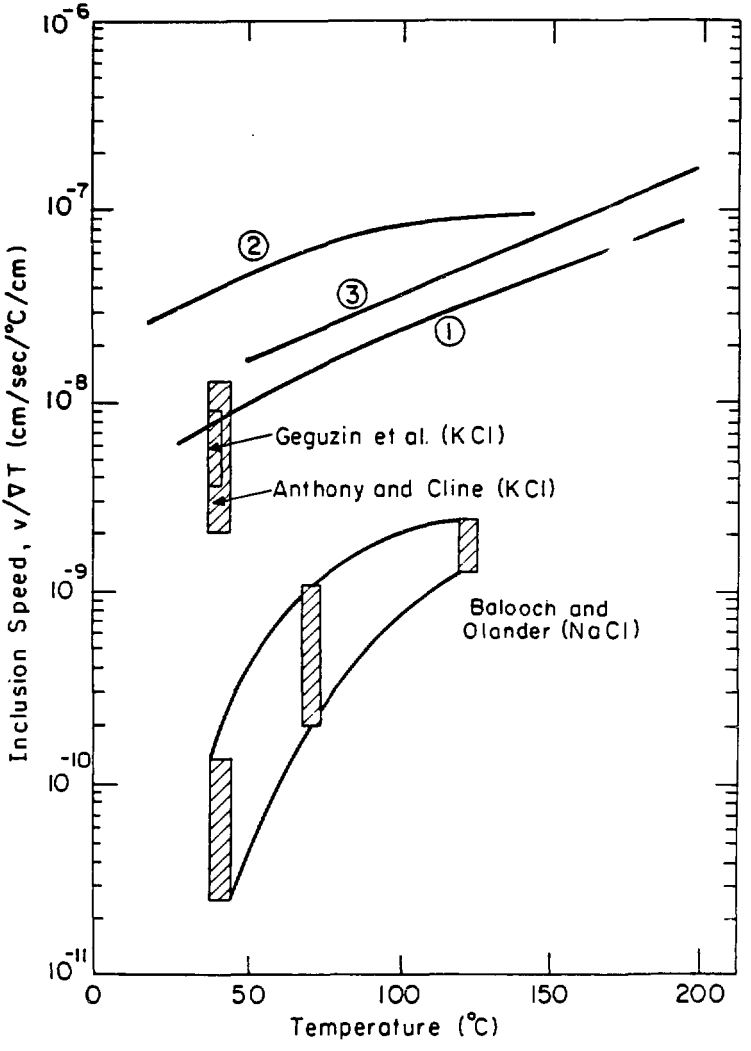

XBL 8010-6069

Fig. 6G. Migration velocities of all-liquid inclusion in NaCl and KCl single crystals as reported by Anthony and Cline, Geguzin et al., and Balooch and Olander. The theoretical diffusion curves and Jenks Equation are also plotted for comparison.

Curves 1 and 2 on Fig. 6G are diffusion limited calculations based on Eq. (4-6) for NaCl and KCl respectively. Curve 3 represents empirical formula proposed by Jenks [39]. Jenks obtained a conservative fit of the data of Bradshaw and Sanchez [40] in the form of the so-called Jenks Equation:

$$\log \frac{V}{\nabla T_{\infty}} = 0.00656T - 0.6036 \qquad (6\text{-}1)$$

This equation is plotted as curve 3 on Fig. 6G.

Since Jenks' curve is based on Bradshaw and Sanchez's [40] data and the theoretical curves are for purely diffusion-limited migration, it follows that the inclusions observed by Bradshaw and Sanchez were in fact moving at this limiting speed. The inclusions studied by Bradshaw and Sanchez were large (typical dimensions of 1 mm) in natural crystals. Even if this material has a dislocation density as low as that of the synthetic single crystals (10^5 cm^{-2}), the faces of each inclusion would have been intersected by ~10^3 dislocations. Diffusion control is therefore expected for the large inclusions, which are intersected by enough dislocations to reduce the kinetic resistance to salt dissolution to negligible values.

Figure 6H shows results from the present work in NaCl single crystal. Four inclusions (J, K, L, M) were followed at low load. Like the inclusions in KCl single crystals, these inclusions too migrated at velocities far lower than the diffusion control limits. Figure 6H clearly shows a non-linear dependence between v and ∇T_1 as expected. To avoid overlapping of different lines in Fig. 6H, a single line is fitted to velocity data from all four inclusions.

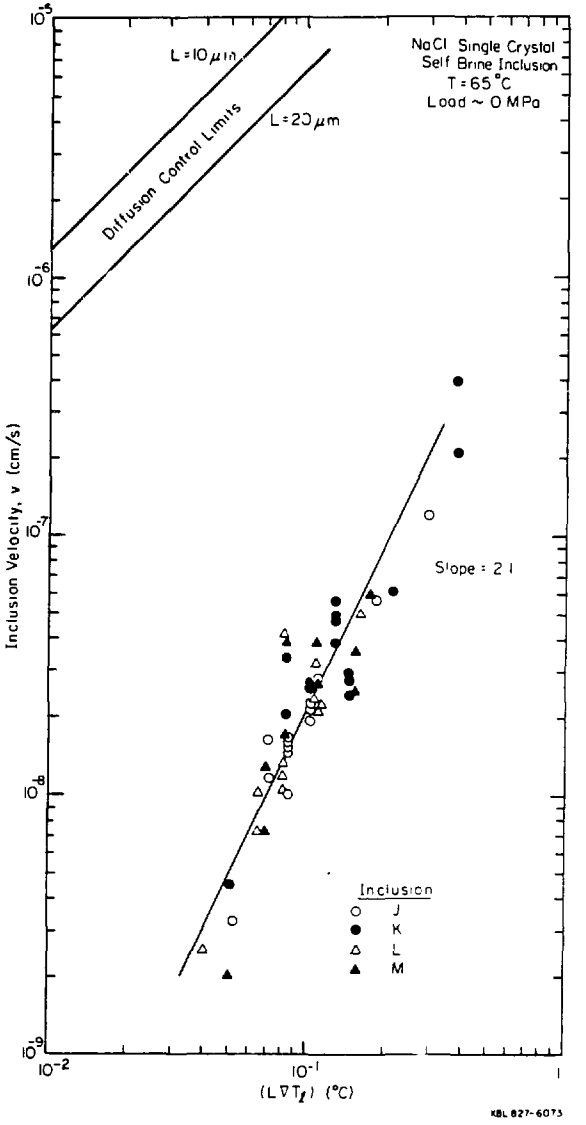

Fig. 6H. Variation of the migration velocity of four inclusions in NaCl with applied temperature gradient. A single line is fitted to Eq. (4-16) for all four inclusions.

The major difference between the single crystal data (both KCl and NaCl) of this work and those of Anthony and Cline [10], Geguzin et al. [11], and Balooch and Olander [38] is that the present work specifically addressed the question of evaluating interfacial kinetics, which needed careful experimental planning. This was accomplished by following only a few selected inclusions at constant temperature while the gradient ∇T_∞ was changed. Shape and size of the inclusions were carefully noted at each experimental observation. Between successive changes of the applied gradient ∇T_∞, the inclusions were allowed to return to their original position by changing the direction of ∇T_∞. When the inclusions returned to their original location, forward migration was resumed with a new ∇T_∞. In this manner all inclusions followed the same "track." Keeping the global temperature of inclusions fixed, and allowing inclusions to follow the same "track," assured that the parameters on which the interfacial kinetic coefficient depends were controlled as best as they could be.

6.1.2.2 Mixed Brine Inclusions

Since inclusions in natural salt contain mixed brines, migration experiments were also done with mixed brine inclusions in NaCl single crystals. For this purpose, inclusions were introduced in two separate samples using 2.1 M $MgCl_2$ and 1M $SrCl_2$ solutions, respectively. The solutions will obviously be saturated by NaCl once inside the crystal in the form of inclusions.

Mixed brine inclusions showed the same behavior as the self-brine in NaCl. The migration speeds were far lower than the diffusion control limits as before. The inherent scatter in velocity data was also observed. The magnitude of migration speeds were about the same as those of self-brine inclusions. The two types of mixed brines (i.e., $MgCl_2$ and $SrCl_2$) showed no difference when compared with one another.

6.1.3 Natural Salt Single Crystals

Fabricated all-liquid inclusions in single crystal samples of natural salt from the Richton Dome behaved much the same way as they did in synthetic NaCl and KCl single crystals.

Figure 6I shows migration speed data for four inclusions (1-4) at different values of applied gradient ∇T_∞ and compares them with the Jenks Equation [Eq. (6-1)]. As expected, Jenks Equation predicts about 2 orders of magnitude higher velocities compared to the experimental data. Also, no observable migration occurred at $\nabla T_\infty \leq 10°C/cm$ even for about a week. This was unlike the case with synthetic single crystals where small but measurable migration took place at $\nabla T_\infty = 10°C/cm$. This can be attributed to higher impurity levels in natural salt compared to the synthetic materials, which is manifest as a minimum gradient for migration or equivalently requires a critical undersaturation for dissolution.

Equation (4-16) was fitted to the data on Fig. 6I and the results appear as a plot of velocity v vs $L\nabla T_1$ in Fig. 6J. All four inclusions show non-linear kinetics. Inclusions 3 and 4 show a large degree of uncertainty in the slope of the fitted curves. This may be due to the fact that inclusion 3 has only four data points and inclusion 4

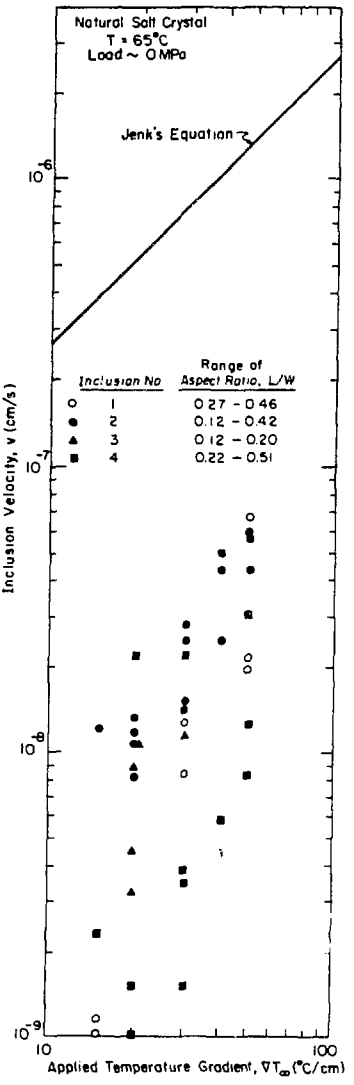

Fig. 61. Variation of migration velocity of four inclusions in a natural salt crystal with the applied temperature gradient.

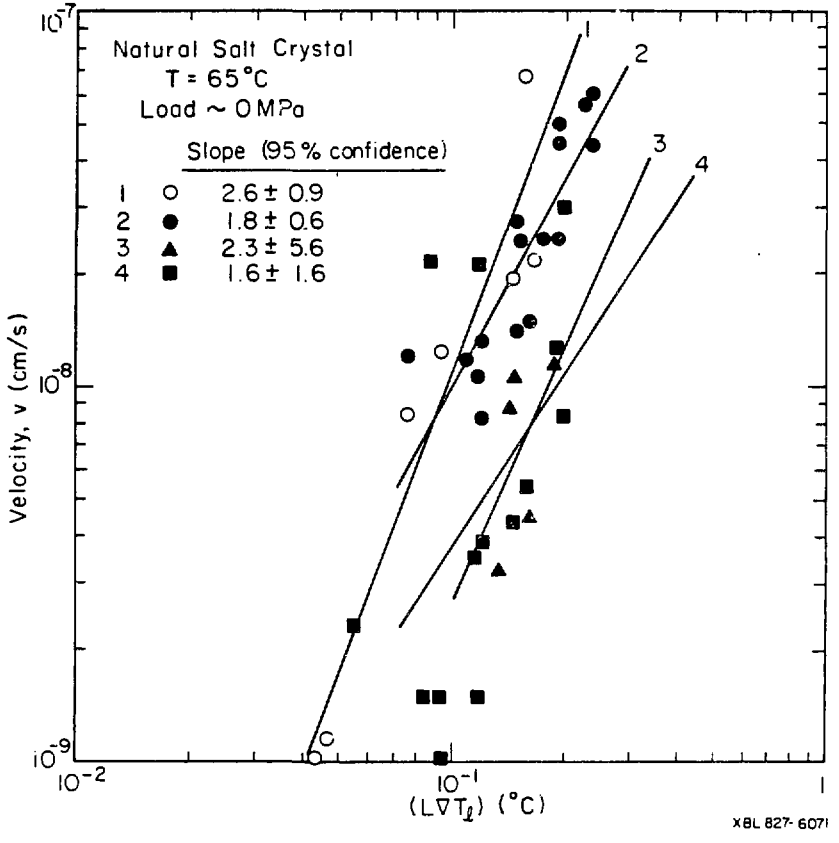

Fig. 6J. Variation of migration velocity of four inclusions in a natural salt crystal with the applied temperature gradient. The lines represent best fit curves from the theory [Eq. (4-16)].

showed an unusually slow movement compared to other inclusions (inclusion 4 could have been pinned down due to local impurity in the natural salt crystal which may have caused measurement errors).

A linear plot of v vs $L\nabla T_1$ for inclusion 2 is shown in Fig. 6K. The plot is clearly parabolic, further confirming the non-linear interfacial kinetics. The other three inclusions also show a parabolic dependence between v and $L\nabla T_1$. Figure 6K indicates a minimum value of $L\nabla T_1$ where the migration ceases.

The response to a sudden increase in compressive mechanical loading produced, as expected, several fold increases in the migration speed of all four inclusions. This behavior is shown in Fig. 6L.

6.2 GAS-LIQUID INCLUSIONS

6.2.1 Transport of Radioactivity

Although it is not certain that gas-liquid inclusions exist at in-situ high pressure (lithostatic) conditions of subsurface salt deposits, microscopic observation of laboratory samples of natural salt verified presence of two-phase inclusions.

Gas-liquid inclusions may also be formed when all-liquid inclusions migrating up the temperature gradient impinge on the wall of the stored wastes [12]. Upon opening up at the salt-canister interface, the brine partially evaporates, the inclusions can reseal with some insoluble gas trapped inside and return down the temperature gradient. In so doing, the inclusion may have picked up some radioactivity from the waste form.

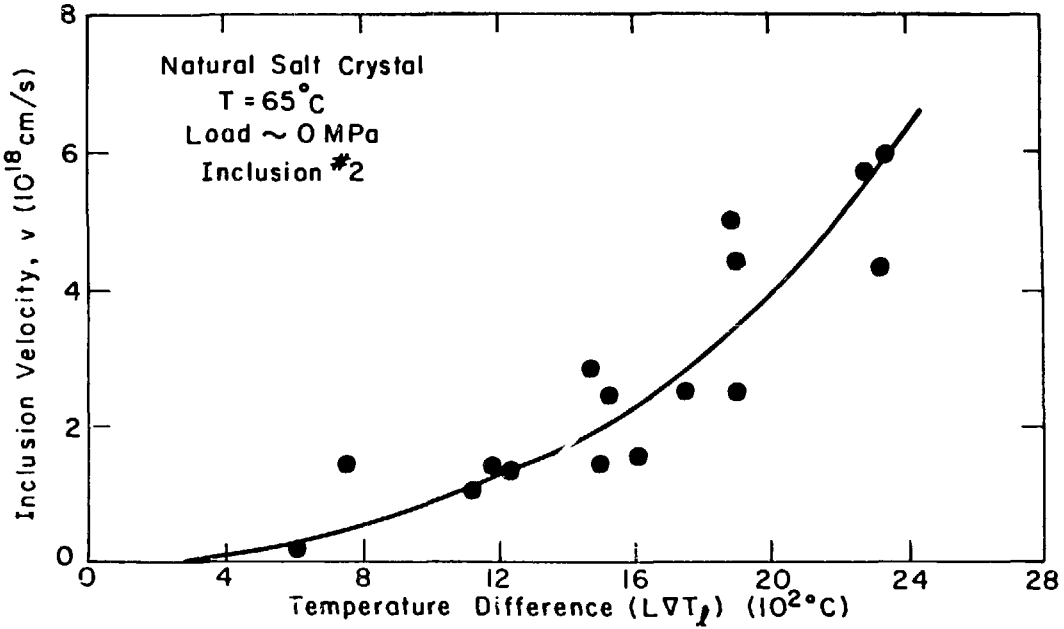

XBL827-6067

Fig. 6K. Linear plot of v vs $L\nabla T_l$ for an inclusion in a natural salt crystal.

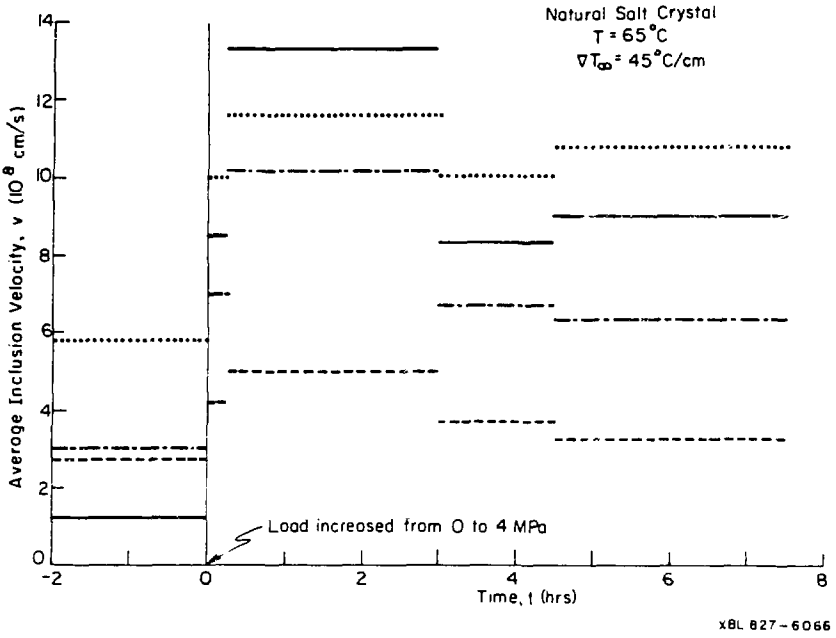

Fig. 6L. Effect of increasing applied axial load on the velocity of four inclusions in natural salt single crystal.

The sequence of events by which an all-liquid inclusion transform into a gas-liquid one and simultaneously picks up radioactivity upon reaching a contaminated wall was experimentally verified as follows:

Twenty-five microlitres of carrier-free Ce^{144} in HCl solution with a specific activity of 20 microcuries/microlitre were evaporated on a thin square copper chip of the size of the crystal end face; the chip was placed between hot copper electrode and crystal face with the contaminated side of the chip contacting the crystal (Refer to Fig. 3B). The salt crystal originally contained a large number of all liquid inclusions. A temperature gradient of 30°C/cm was applied to the crystal for about a month, as a result most all-liquid inclusions reached the hot end of the crystal. Several trails of very small gas-liquid inclusions were observed migrating down the gradient; however, a clear one-to-one conversion of an all-liquid inclusion arriving at the hot end into a gas-liquid inclusion was not observed.

The crystal was counted before and after the above procedure. Surface contamination on the crystal surface was removed prior to the counting. The residual counts could be attributed to Ce^{144} transported into the crystal via gas-liquid inclusions which appeared as the all-liquid inclusions began to arrive at the hot end of the crystal.

6.2.2 Comparison of Different Gas Phases

According to the theoretical model of Olander et al. [13], the migration velocity of a gas-liquid inclusion depends, among other parameters, on the inert gas phase itself. Since the diffusivity of water vapor through the central gas bubble depends on the gas phase proper-

ties, and the thermal conductivity of the bubble affects the temperature distribution in the brine, it follows that when the inert gas phase is changed (from air to helium, for example) a different velocity is theoretically expected.

Figure 6M shows theoretical and experimental velocities of air-water inclusions in NaCl from Olander et al. [13]. The two sets of curves (solid and dotted) are respectively with and without the interfacial resistance at the solid/brine interface accounted for in the theory. The interfacial resistance, which is based on the all-liquid inclusion data from Ref. [9], lowers the theoretically predicted velocities by an order of magnitude as compared to the case of no interfacial mass transfer resistance at solid/brine interface. The vertical bars represent the data on a number of inclusions of various size and volume fraction of gas. It is evident from the experimental data that like all-liquid inclusions, interfacial kinetics are important for gas-liquid inclusions as well. Notice that the bubble size in calculating the theoretical curves in Fig. 6M is taken to be 11.2 μm, the mean size for the experimentally observed inclusions.

The effect of changing the gas phase as predicted by the theory is shown in Fig. 6N. The curves show migration velocity per unit temperature gradient for an inclusion of given volume fraction gas and bubble size. The theory predicts that the migration speed of the helium-water inclusion should be about 6 times that of the argon-water inclusion at 50°C and about 3 times at 100°C.

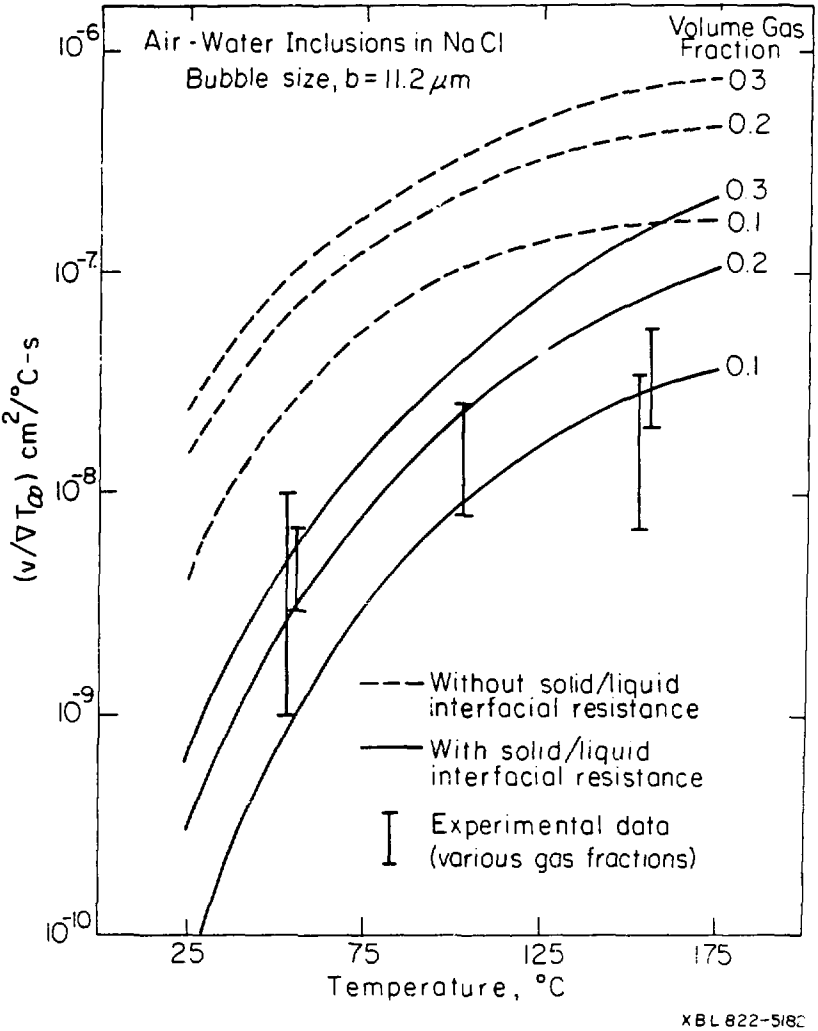

Fig. 6M. Migration velocity of air-water inclusions in NaCl single crystal as predicted by the approximate model of Olander et al. The bars represents the experimental data for various gas fractions and bubble size.

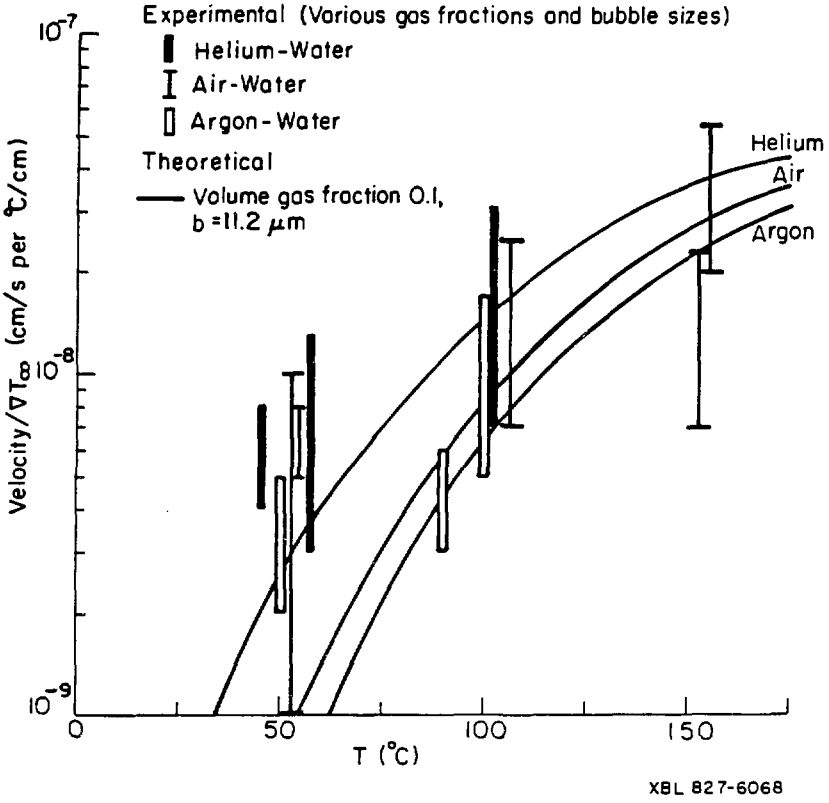

Fig. 6N. Comparison of three different gas phase inclusions in NaCl single crystal.

The experimental data of helium-water and argon-water (this work), and air-water (Ref. [13]) are also shown superimposed on Fig. 6N as vertical bars. The data were obtained for a number of inclusions with different values of gas fraction and bubble size, whereas, the theoretical curves are for specific values of these parameters (i.e., $b = 11.2$ μm and volume fraction 0.1) with a best fit value of interfacial coefficient k from the all-liquid inclusion data. It was not possible to control the bubble size and gas fraction to predetermined values, which limits a meaningful graphical comparison of the data and the theory. Nonetheless, the trend of $v_{helium} > v_{air} > v_{argon}$ is clear from the data.

6.3 INCLUSIONS AT GRAIN BOUNDARIES

In a bi-crystal sample fabricated of natural salt, several naturally occurring all-liquid and gas-liquid inclusions were observed attached to the large angle grain boundary. Figure 6O and 6P show these grain boundary inclusions at different locations on the grain boundary. A rough estimate showed that the fluid at the grain boundary constituted a maximum of 0.3 vol percent in the sample.

The direction of experimentally observed migration of grain boundary inclusions under an applied temperature gradient was as expected (i.e., the all-liquid inclusions moved up the gradient and the gas-liquid inclusions moved down the gradient). The migration, however, did not take place in straight lines parallel to the direction of the temperature gradient. Unlike the inclusions in the single crystals, the grain boundary inclusions migrated by two-dimensional movements in a plane (the inclusions remain in the same plane of focus when observed

Fig. 60. All-liquid inclusions at a large angle grain boundary in natural salt sample (shown by arrows).

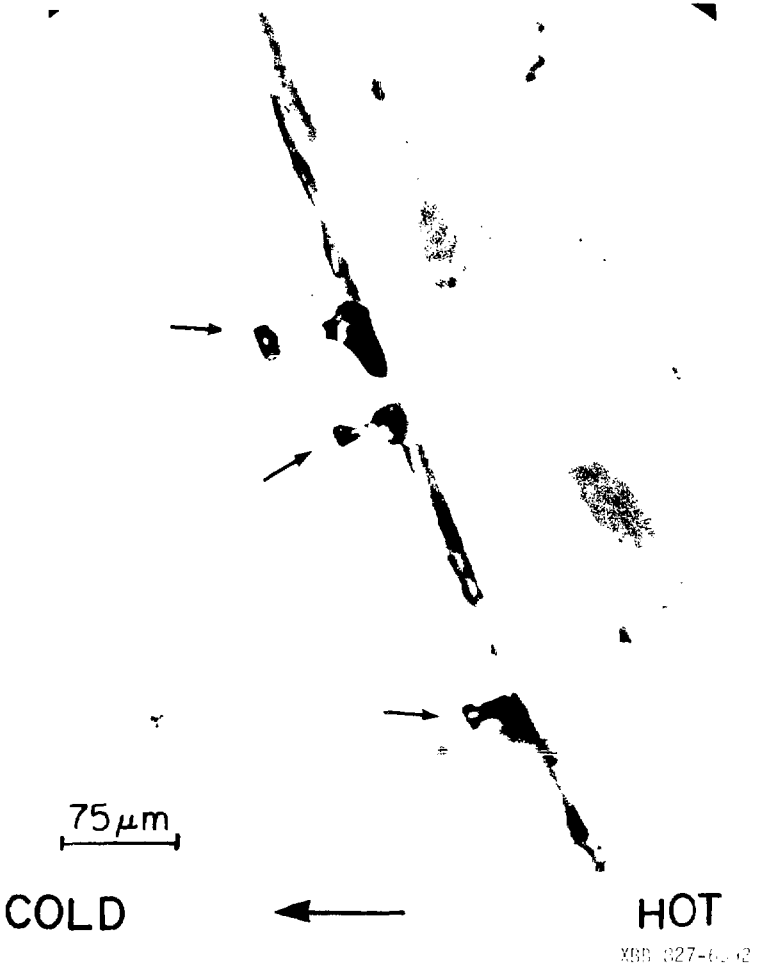

XBB 827-6042

Fig. 6P. Gas-liquid inclusions at a large angle grain boundary in natural salt sample (shown by arrows).

through the optical microscope) with a net drift up or down the gradient depending on the type of inclusion.

For an all-liquid inclusion marked by the X in Fig. 6O, the scenario just described is depicted in Fig. 6Q. The coordinates of a sharp corner of this inclusion are plotted in Fig. 6Q with respect to an arbitrary reference point as the origin. The grain boundary coincides with the y-axis. The numbers in parentheses indicate the time (in hours) of each observation starting from the initial position at t = 0 hrs. Successive positions of the inclusion in the plane of migration are joined by straight lines. These do not imply that the locus of migration between two successive readings was actually a straight-line. From Fig. 6Q, it is evident that the inclusion followed has a general tendency to move up the gradient, although not in a straight line. Several other grain boundary inclusions showed similar behavior. Once the inclusions moved far away from the grain boundary, they behaved in much the same way as single crystal inclusions.

The erratic two dimensional migration of inclusions at and near a grain boundary can be attributed, in part, to the large mismatch between the grains which must exist at a large angle grain boundary. The solid lattice at the grain boundary is highly distorted. The grain boundary inclusion, migrating by dissolution-crystallization mechanism, seeks to conform to {100} planes, although the temperature gradient is applied clearly in a direction other than <100>. This was confirmed by several inclusions which were platelet shaped far from the grain boundary, but tended to become chevron-shaped as they approached it.

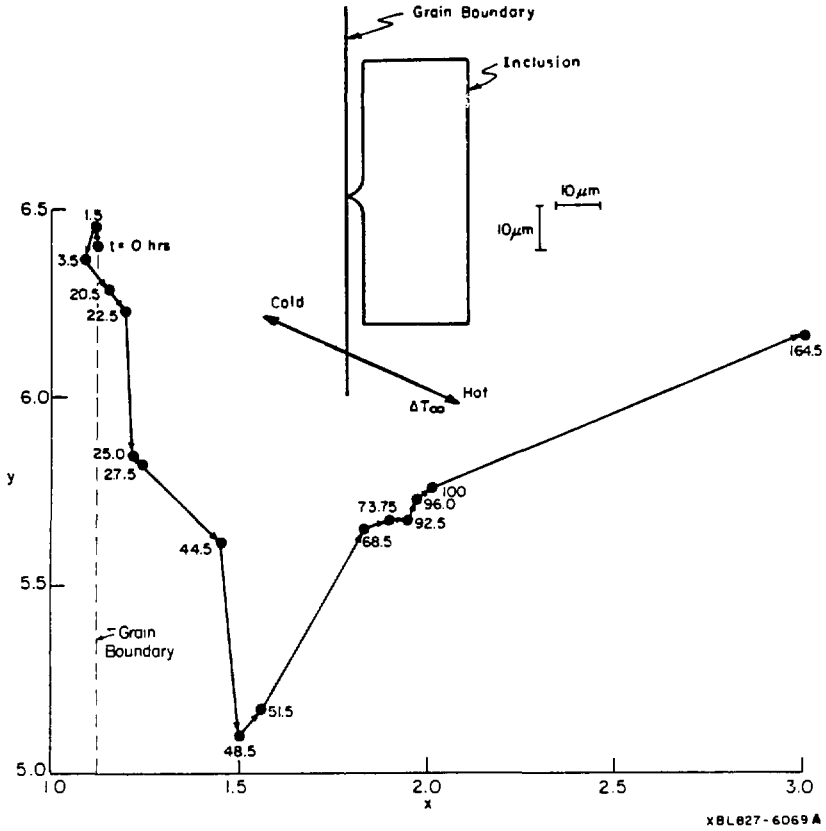

Fig. 6Q. Two dimensional motion of an all-liquid inclusion at and near a large angle grain-boundary in natural salt sample supporting a temperature gradient.

Finally, since an inclusion at a grain boundary is in a position of minimum energy, it tends to glide along the grain boundary from cold to hot regions (or hot to cold for gas-liquid inclusions) rather than detach itself completely from the grain boundary. This is seen in the behavior of the inclusion in Fig. 6Q for times up to ~27 hours.

CHAPTER 7

CONCLUSIONS

Temperature gradient migration of intragranular all-liquid and gas-liquid inclusions in salt crystals has been examined experimentally and theoretically. An optical microscope hot stage attachment capable of nonuniformly heating and mechanically loading the salt sample was used for this purpose.

Micron-size inclusions in synthetic as well as natural single crystals showed that the slow interfacial step, which is probably associated with dissolution at the hot face of the inclusion, is more important than liquid diffusion as a resistance to salt transport, hence in determining the migration velocities.

The migration velocity varies approximately as the square of the temperature gradient rather than linearly as suggested by the theory of Anthony and Cline, and Geguzin et al. The nonlinear dependence is in accord with the Burton-Cabrerra-Frank (BCF) model of crystallization catalyzed by dislocations emerging at the interface. Because of the small sizes of the inclusions produced in synthetic single crystals and the low dislocation density of this material, the dissolving faces of the inclusions are intersected by a small number of dislocations. Random variations in this number account for significant variations in the velocity of a single inclusion with time and for the scatter in the velocities measured for a number of different inclusions subjected to the same conditions. When the dislocation population is increased by mechanical stressing, the migration velocity increases dramatically. In general, the rate-limiting process in thermal gradient

migration of inclusions in brine depends both on the size of the inclusion and on the dislocation density of the solid in which it moves. Diffusion control is expected for inclusions large enough to be intersected by a large number of defects. When interfacial kinetics is controlling, the variation of the inclusion speed with the temperature gradient, the large variability of inclusion speeds measured under identical macroscopic conditions, and the effect of mechanical loading of the crystal on the speed are best rationalized by the BCF model.

Interfacial stability of a migrating all-liquid inclusion is treated theoretically. The temperature gradient tends to force an inclusion to take up a roughly spherical shape but the great stability of low index {100} planes, and the layer by layer growth/dissolution principle, keep the inclusion boundaries sharp with {100} faces.

All-liquid inclusions in natural salt single crystals also show interfacial kinetic controlled migration with velocities at least two orders of magnitude lower than those given by Jen.s Equation.

For gas-liquid inclusions, the approximate analytical model of Olander et al. was tested by comparing the migration of helium-water, air-water, and argon-water inclusions. The general trend, predicted theoretically, that the migration velocity should decrease as the air is replaced by heavier argon, and increase as it is replaced by lighter helium, was confirmed experimentally.

In a real repository in natural salt, both intragranular and intergranular water will be mobilized when salt is subjected to a temperature gradient. The intragranular inclusions will eventually reach

grain-boundaries under the influence of the temperature gradient. The fate of the inclusions and the accompanying water at the grain-boundaries is not quite clear. If one considers the grain-boundaries to be very "tight," such as can be fabricated by sintering two single crystals, the intragranular water driven by the thermal gradient will be impeded by the grain-boundary tension. Large temperature gradient will be necessary in such a case to pull away the inclusions from a grain-boundary.

On the other hand, it is likely that the grain-boundaries in natural salt deposits will be weakened by the mechanical action of boring drillhole and subsequent release of lithostatic pressure on salt. The grain-boundaries are thus rendered permeable and the intergranular brine may escape through these grain-boundary pores.

The migration studies in synthetic and natural single crystals reported in this work provide basic understanding of mechanism of inclusion migration. However, unlike single crystals, the natural salt is polycrystalline with high levels of impurities and imperfections. It is therefore important to extend the migration experiments in natural salt specimens.

A polycrystalline natural salt sample to be used in a laboratory for migration studies has to be far larger than the sample size used in this work. This is because typical grain size in salt is about 1 cm. To get a fair representation of grain boundary effect, the samples must be at least several centimeters in size. For such samples, the optical microscope method can not be used due to the following reasons:

(i) The high levels of impurities and imperfections in natural salt together with the size requirements make the samples opaque. Even the chemical polishing turns them only semi-transparent at best, making it very difficult to observe inclusions within the samples.

(ii) The second reason has to do with the optical limitations of the microscope. At high magnifications necessary to optically observe inclusions, the distance between the point of focus and the objective lens of the microscope is quite small, generally 1 to 5 mm. Since the sample must be at least 1 cm in height due to the grain size requirement, it is obviously not possible to observe the whole interior of the sample without the objective lens hitting the top surface of the sample.

Due to the above reasons, a radioactive tracer technique to monitor the migration must be developed. This method tags the migrating brine within the sample with an inert radioactive material and the migration itself is observed by radioactive detectors rather than the optical microscope.

APPENDIX A

TEMPERATURE GRADIENTS IN ALL-LIQUID INCLUSION

In Chapter 3 the global temperature of an inclusion within the salt crystal was discussed. This temperature is calculated by the linear interpolation of experimentally established end temperatures of the salt crystal. Physical property data needed in the velocity expression [Eq. (4-16)] are calculated at this global temperature of the inclusion.

In a microscopic sense, on the other hand, a square platelet-shaped inclusion embedded in a solid supporting an external temperature gradient, has a more complicated temperature field. A complete temperature distribution inside the inclusion can be obtained as a function of the aspect ratio by solving Laplace's equation in both solid and liquid and using heat flux and temperature continuity conditions at the cavity boundaries. Numerical solutions obtained with the code HEATING5 are shown in Fig. A1 in terms of a thermal gradient amplification factor defined by

$$\mathcal{A} = \nabla T_l / \nabla T_\infty . \qquad \text{(A-1)}$$

This factor is a function of the aspect ratio of the inclusion L/W and the off-axis position X. On the axis of the inclusion, the amplification factor is bounded by

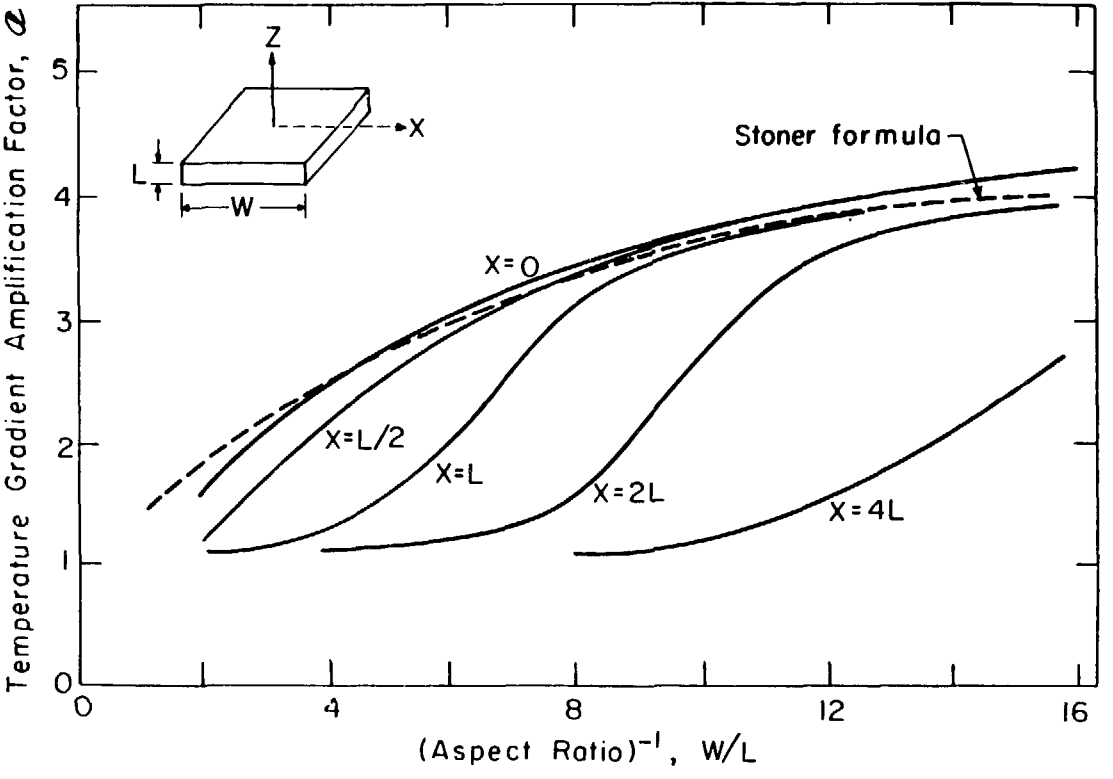

XBL 8010-6067

Fig. A1. Temperature gradient amplification factor in an all-liquid inclusions.

$$\mathcal{A}(X = 0) = \begin{cases} 3/(2 + k_l/k_s) & \text{for } L/W = 1, \\ k_s/k_l & \text{for } L/W = 0, \end{cases} \tag{A-2}$$

where k_s and k_l are the thermal conductivities of the solid and liquid, respectively; their ratio is ~7 for NaCl and ~10 for KCl. The value of the amplification factor for the cubical inclusion is essentially equal to that for a sphere. The formula obtained by Stoner [26] for prolate spheroids,

$$\mathcal{A}(X = 0) = [(1 - F) + F(k_l/k_s)]^{-1} \quad , \tag{A-3}$$

where

$$F = \frac{1}{1 - (L/W)^2} \left\{ 1 - \frac{(L/W)\cos^{-1}(L/W)}{[1 - (L/W)^2]^{1/2}} \right\} \tag{A-3}$$

has been used to represent the gradient on the axis of the square platelets. Note that Eqs (A-3) and (A-4) exhibit the limiting behavior indicated by Eq. (A-2).

The variation of the thermal gradient amplification factor with off-axis location is just as important as its dependence upon the inclusion aspect ratio. Figure A1 shows that $\mathcal{A}$ is largest on the axis ($X = 0$) but decreases to unity at the edge of the inclusion ($X = W/2$). For example, consider an inclusion in NaCl with an aspect ratio L/W of 1/6. It can be seen from Fig. A1 that the temperature gradient on the inclusion axis is ~3 times larger than ∇T_∞, but at 1/3 of the distance between the axis and the edge ($X = L$), the amplification factor has been reduced to ~2. At two-thirds of the way to the edge ($X = 2L$),

∇T_1 is approximately equal to ∇T_∞. In this particular example, there is an uncertainty (or variation) of a factor of 3 in relating ∇T_1 to ∇T_∞.

APPENDIX B

IMPURITY EFFECT AND THE ORDER OF INTERFACIAL KINETICS

In this appendix the limiting cases of Eq. (4-16) are derived. It is also shown that the value of exponents relating v and $L\nabla T_1$ which are higher than 2 are due to non-zero values of ξ^*. In other words, impurity effects discussed in Section 4.1.2.3 which are manifest as a critical undersaturation for dissolution ξ^*, predict that v should increase with $L\nabla T_1$ more rapidly than $(L\nabla T_1)^2$.

Equation (4-16) can be written as

$$v = A\mathcal{D}\left[\left\{\sqrt{(1-x)^2 + \frac{4L\nabla T_1}{\mathcal{D}}B} - 1\right\}^2 - x^2\right] \qquad \text{(B-1)}$$

where

$$A = \frac{D_1 C^{sat}}{4L\rho_s}$$

$$B = \left(\frac{1}{C^{sat}}\frac{dC^{sat}}{dT} - \sigma\right)$$

$$x = \frac{\xi^*}{\mathcal{D}}$$

$$\mathcal{D} = \frac{D_1 C^{sat}}{kL}$$

Diffusion Controlled Limit:

When diffusion is slow and rate controlling, and interfacial mass transfer is rapid, the coefficient k is very large and undersaturation ξ^* is very small. Thus $x = 0$ and $\mathcal{D}$ is sufficiently small so that $\frac{4L\nabla T_1}{\mathcal{D}} B >> 1$. Equation (B-1) can then be written as

$$v = A\mathcal{D}\left\{\sqrt{\frac{4L\nabla T_1}{\mathcal{D}}\,B - 1}\right\}^2 \approx 4L\nabla T_1\, AB \qquad (B\text{-}2)$$

Substituting A and B into (B-2) yields

$$v = \frac{D_1 C^{sat}}{\rho_s}\left(\frac{1}{C^{sat}}\,\frac{dC^{sat}}{dT} - \sigma\right)\nabla T_1 \qquad (B\text{-}3)$$

Equation (B-3) is the same as Eq. (4-6) which gives purely diffusion controlled migration velocity for an inclusion.

Interfacial Controlled Limit

When diffusion is fast but interfacial mass transfer is slow and rate controlling, the diffusivity D_1 is large but interfacial coefficient k is small. Thus, the dimensionless parameter $\mathcal{D}$ is large and two limiting cases, with and without a critical undersaturation due to impurities are considered separately.

Case 1: No Impurity Effect

For growth/dissolution in a pure crystal, surface diffusion growth theory (see section 4.1.2.2) does not predict existence of critical undersaturation or supersaturation. Therefore, in this case $\xi^* = 0$ and hence $x = 0$. Equation (B-1) then becomes

$$v = A\mathcal{D}\left[\left\{1 + \frac{4L\nabla T_1}{\mathcal{D}}\,B\right\}^{1/2} - 1\right]^2 \qquad (B\text{-}4)$$

Since $\mathcal{D}$ is large, the bracketed terms can be written by the series expansion

$$v = A\mathcal{D}\left[1 + \frac{1}{2}\frac{4L\nabla T_1}{\mathcal{D}}B + \text{---} - 1\right]^2$$

Substituting A and B in the above equation and simplifying yields

$$v = \frac{k}{\rho_s}\left(\frac{1}{C^{sat}}\frac{dC^{sat}}{dT} - \sigma\right)^2 (L\nabla T_1)^2 \qquad \text{(B-5)}$$

Equation (B-5) is the same as Eq. (4-17) which gives purely interfacial controlled migration velocity for an inclusion. The exponent of 2 for $(L\nabla T_1)$ encompasses the BCF theory.

Case 2: Impurity Effect

Impurity effects, discussed in section 4.1.2.3, are manifest as a critical undersaturation or supersaturation. Therefore, in this case, $\xi^* \neq 0$.

For $\xi^* \neq 0$, v varies with $L\nabla T_1$ with a power greater than 2, as can be demonstrated by differentiating Eq. (B-1) with respect to $(L\nabla T_1)$.

$$\frac{dv}{d(L\nabla T_1)} = A\mathcal{D}\,2\left[\sqrt{1-2x+x^2+\frac{4B}{\mathcal{D}}L\nabla T_1} - 1\right] \cdot \frac{1}{2}\left\{1 - 2x + x^2 + \frac{4B}{\mathcal{D}}L\nabla T_1\right\}^{-1/2} \cdot \frac{4B}{\mathcal{D}} \qquad \text{(B-6)}$$

On a log-log plot one is interested in the slope given by

$$\frac{d(\ln v)}{d(\ln(L\nabla T_1))} \cdot$$

Since

$$\frac{d(\ln v)}{d(\ln(L\nabla T_1))} = \frac{L\nabla T_1}{v}\frac{dv}{d(L\nabla T_1)} \qquad \text{(B-7)}$$

Substituting $\frac{dv}{d(L\nabla T_1)}$ from Eq. (B-6) into Eq. (B-7), and using Eq. (B-1)

results in $\frac{d\ln v}{d(\ln(L\nabla T_1))} =$

$$\frac{\left[\sqrt{1-2x+x^2+\frac{4B}{\mathcal{D}}L\nabla T_1}-1\right]\cdot\frac{4B}{\mathcal{D}}L\nabla T_1}{\left\{1-2x+x^2+\frac{4B}{\mathcal{D}}L\nabla T_1\right\}^{1/2}\cdot\left[\left\{\sqrt{1-2x+x^2+\frac{4L\nabla T_1}{\mathcal{D}}B}-1\right\}^2-x^2\right]} \quad \text{(B-8)}$$

Since $x = \frac{\xi^*}{\mathcal{D}}$, and $\mathcal{D}$ is very large, the value of x is small but non-zero. Therefore, in this case $\left[-2x+x^2+\frac{4L\nabla T_1}{\mathcal{D}}B\right] \ll 1$. Thus, the term under the square root sign in the numerator and the denominator of Eq. (B-8) can be expanded and the result is

$$\frac{d(\ln v)}{d(\ln(L\nabla T_1))} = \frac{\frac{4BL\nabla T_1}{\mathcal{D}}\left[1-x+\frac{x^2}{2}+\frac{2B}{\mathcal{D}}L\nabla T_1+\cdots-1\right]}{1\cdot\left[\left\{1-x+\frac{x^2}{2}+\frac{2B}{\mathcal{D}}L\nabla T_1+\cdots-1\right\}^2-x^2\right]}$$

or,

$$\frac{d(\ln v)}{d[\ln(L\nabla T_1)]} = \frac{\frac{4BL\nabla T_1}{\mathcal{D}}\left[-x+\frac{x^2}{2}+\frac{2BL\nabla T_1}{\mathcal{D}}\right]}{\left[\frac{x^2}{2}+\frac{2BL\nabla T_1}{\mathcal{D}}\right]\left[-2x+\frac{x^2}{2}+\frac{2BL\nabla T_1}{\mathcal{D}}\right]} \cdot \quad \text{(B-9)}$$

Neglecting x^2 terms in Eq. (B-9) gives

$$\frac{d\ln v}{d[\ln(L\nabla T_1)]} \simeq 2\,\frac{-x+\frac{2BL\nabla T_1}{\mathcal{D}}}{-2x+\frac{2BL\nabla T_1}{\mathcal{D}}} = 2\left[\frac{1-\frac{1}{2}\frac{\xi^*}{BL\nabla T_1}}{1-\frac{\xi^*}{BL\nabla T_1}}\right] \cdot \quad \text{(B-10)}$$

For $\xi^*/BL\nabla T_1 < 1$, the square bracketed term on the right hand side of (B-10) is always greater than unity. Typical values for the term $(\xi^*/BL\nabla T_1)$ for NaCl and KCl are ~0.01. Thus, with impurity effect applicable, exponents of $(L\nabla T_1)$ which are greater than 2 are expected.

In the limit of $\xi^* \longrightarrow 0$ (i.e., interfacial controlled migration without impurity effect), the square bracketed term on the right hand side of (B-10) reduces to unity. Then v varies as $(L\nabla T_1)^2$ as expected.

REFERENCES

[1] "Nuclear Chemical Engineering" by M. Benedict, T. Pigford and H. Levi, Second Edition, Chapter 11, McGraw Hill Book Company, New York (1981).

[2] D. J. Isherwood, "Fluid Inclusions in Salt: An Annotated Bibliography," UCID-18102, Lawrence Livermore Laboratory (1979).

[3] E. Roedder and H. E. Belkin, "Application of Studies of Fluid Inclusions in Permian Salt, New Mexico, to Problems of Siting the Waste Isolation Pilot" in Scientific Basis for Nuclear Waste Management, vol. 1, 313 (1980). Editor: G. J. McCarthy.

[4] G. H. Jenks and H. C. Claiborne, "Brine Migration in Salt and its Implications in the Geologic Disposal of Nuclear Waste," ORNL-5818, Oak Ridge National Laboratory, (1981).

[5] W. T. Holser, "Chemistry of Brine Inclusions in Permian Salt from Hutchinson, Kansas." Symposium on Salt, Northern Ohio Geologic Society, Inc., Cleveland, Ohio, pp. 86-95 (1963).

[6] J. Lorenz et al., "Geology, Mineralogy, and Some Geophysical and Geochemical Properties of Salt Deposits," in Physical Property Data for Rock Salt, NBS-167, National Bureau of Standards Monograph (1981).

[7] "Fundamental Aspects of Nuclear Reactor Fuel Elements," by D. R. Olander, Chapter 14, TID-26711-P1, Technical Information Centre, Energy Research and Development Administration (1976).

[8] "Migration of Macroscopic Inclusions in Solids," by Ya. E. Geguzin and M. A. Krioglaz, translated from Russian, Studies in Soviet Sciences, Consultants Bureau, New York (1973).

[9] D. R. Olander et al., "Thermal Gradient Migration of Brine Inclusions in Synthetic Alkali Halide Crystals," J. Appl. Phys., 53, 669 (1982).

[10] T. R. Anthony and H. E. Cline, "Thermal Migration of Liquid Droplets through Solids," J. Appl. Phy., 42, 3380 (1971).

[11] Ya. E. Geguzin et al., "Response to a Temperature Gradient from Liquid Inclusions in a Crystal," Sov. Phy. Crystallogr. 20, 234 (1975).

[12] T. R. Anthony and H. E. Cline, "The Thermomigration of Biphase Vapor Liquid Droplets through Solids," Acta Met. 20, 247 (1972).

[13] D. R. Olander et al., "Migration of Gas Liquid Inclusions in Single Crystals of Potassium and Sodium Chloride," Nuclear Science and Engineering, 79, 212 (1981).

[14] W. F. Johnston, "Dislocation Etch Pits in Non-Metallic Crystals," in Prog. Cer. Sci., Vol. 2, 1 (1961). Editor: J. E. Burke, Pergamon Press, New York.

[15] S. Mendelson, "Dislocation Etch Pits Formation in Sodium Chloride," J. Appl. Phy. 32, 1579 (1961).

[16] P. R. Moran, "Dislocation Etch Techniques for Some Alkali Halide Crystals," J. Appl. Phy. 29, 1768, (1963).

[17] H. E. Cline and T. R. Anthony, "Effects of the Magnitude and Crystallographic Direction of a Thermal Gradient on Droplet Migration in Solid," J. Appl. Phy. 43, 10 (1972).

[18] "Modeling Crystal Growth Rates from Solutions," by M. Ohara and R. C. Reid, Chapter 4, Prentice Hall, Englewood Cliffs, N.J. (1973).

[19] "Kinetics and Mechanism of Crystallization," by R. F. Strickland-Constable, Chapter 6, Academic Press, London (1968).

[20] F. C. Frank, "The Influence of Dislocations on Crystal Growth". Discuss. Faraday Society, 5, 48 (1949).

[21] G. D. Botsaris, "Effects of γ-Irradiation and Additives on Growth of Potassium Chloride Crystals from Aqueous Solutions," Ph.D. Thesis, Massachusetts Institute of Technology (1965).

[22] A. J. Machiels, "Impurities and Inclusion Size Effects on the Migration Velocity of Liquid Inclusion in Salt," (unpublished).

[23] W. R. Wilcox, "The Role of Mass Transfer in Crystallization Process," in Preparation and Properties of Solid State Materials," vol. 1, 37 (1971). Editor R. A. Lefever, Dekker, New York.

[24] T. H. Pigford, "Migration of Brine Inclusions in Salt," UCB-NE-4001, University of California, Berkeley (1981).

[25] T. R. Anthony and H. E. Cline, "The Stability of Migrating Droplets in Solids," Acta Met., 21 117, (1973).

[26] E. C. Stoner, "The Demagnetization Factors for Ellipsoids," Phil. Mag. 36, Ser 7, 803 (1945).

[27] W. W. Mullins and R. F. Sekerka, "Morphological Stability of a Particle Growing by Diffusion or Heat Flow," J. Appl. Phys., 34, 323 (1963).

[28] W. W. Mullins and R. F. Sekerka, "Stability of Planar Interface During Solidification of a Dilute Binary Alloy," J. Appl. Phys., 35, 444 (1964).

[29] G. R. Kotlier and W. A. Tiller, "The Effect of Interface Attachment Kinetics on the Perturbation Analysis of a Cylinder Crystallizing from a Binary Alloy Melt," in Crystal Growth, pp. 721-732 (1967). Editor: H. S. Peiser, Pergamon Press, New York.

[30] R. F. Sekerka, "A Time-Dependent Theory of Stability of a Planar Interface During Dilute Binary Alloy Solidification," in Crystal Growth, pp. 691-702 (1967) Editor: H. S. Peiser, Pergamon Press, New York.

[31] R. F. Sekerka, "Morphological Stability," J. Cryst. Growth, 3, 71 (1968).

[32] R. T. Delves, "Theory of Interface Stability" in Crystal Growth, pp. 40-103 (1975). Editor: B. R. Pamplin, Pergamon Press, New York.

[33] R. G. Seidensticker, "Stability Considerations in Temperature Gradient Zone Melting," in Crystal Growth, pp. 733-737 (1967). Editor: H. S. Peiser, Pergamon Press, New York.

[34] D. R. Olander et al., "Thermal Gradient Migration of Brine Inclusions in Salt," ONWI-208, Office of Nuclear Waste Isolation, Battelle, Columbus, Technical Report (1980).

[35] J. Garside, "Kinetics of Crystallization from Solution," in Current Topics in Material Science, Vol. 2, 484 (1977). Editor: E. Kaldis, North Holland, Amsterdam.

[36] P. J. Lemaire and H. K. Bowen, "Migration of Small Pores in Potassium Chloride due to a Temperature Gradient," J. Amer. Cer. Soc., 65, 49 (1982).

[37] P. Bennema and G. H. Gilmer, "Kinetics of Crystal Growth," in Crystal Growth: An Introduction, 263 (1973). Editor: P. Hartman, North Holland, Amsterdam.

[38] M. Balooch and D. R. Olander, "Migration of Brine Inclusions in Single Crystals of NaCl," LBL-10252, Lawrence Berkeley Laboratory, Berkeley (1979).

[39] G. H. Jenks, "Effects of Temperature, Temperature Gradients, Stress, and Irradiation on Migration of Brine Inclusions in a Salt Repository," ORNL-5526, Oak Ridge National Laboratory, Oak Ridge (1979).

[40] R. L. Bradshaw and F. Sanchez, "Brine Migration Studies," ORNL-4316, Oak Ridge National Laboratory, Oak Ridge (1968).